Optimization of Low Reynolds Number Airfoils for Martian Rotor Applications Using an Evolutionary Algorithm

Witold J. F. Koning[*]

Science and Technology Corporation, NASA Ames Research Center, Moffett Field, California 94035

Ethan A. Romander[†] and Wayne Johnson[‡]

NASA Ames Research Center, Moffett Field, California 94035

For invited session Special Joint AIAA-JSASS Session on Martian Aerodynamics
Chairs: Maziar Hemati, Taku Nonomura, and Kunihiko Taira

The Mars Helicopter (MH) will be flying on the NASA Mars 2020 rover mission scheduled to launch in July of 2020. Research is being performed at the Jet Propulsion Laboratory (JPL) and NASA Ames Research Center to extend the current capabilities and develop the Mars Science Helicopter (MSH) as the next possible step for Martian rotorcraft. The low atmospheric density and the relatively small-scale rotors result in very low chord-based Reynolds number flows over the rotor airfoils. The low Reynolds number regime results in rapid performance degradation for conventional airfoils due to laminar separation without reattachment. Unconventional airfoil shapes with sharp leading edges are explored and optimized for aerodynamic performance at representative Reynolds-Mach combinations for a concept rotor. Sharp leading edges initiate immediate flow separation, and the occurrence of large-scale vortex shedding is found to contribute to the relative performance increase of the optimized airfoils, compared to conventional airfoil shapes. The oscillations are shown to occur independent from laminar-turbulent transition and therefore result in sustainable performance at lower Reynolds numbers. Comparisons are presented to conventional airfoil shapes and peak lift-to-drag ratio increases between 17% and 41% are observed for similar section lift.

I. Nomenclature

B	Bézier curve (vector of coordinates)
c	airfoil chord
c_d	section drag coefficient, $c_d \equiv \frac{D}{(1/2)\rho_\infty U_\infty^2 c}$
c_d^*	reference section drag coefficient
$c_{d_{min}}$	minimum section drag coefficient
c_{d_μ}	mean section drag coefficient
c_l	section lift coefficient, $c_l \equiv \frac{L}{(1/2)\rho_\infty U_\infty^2 c}$
c_l^*	reference section lift coefficient
$c_{l_{max}}$	maximum section lift coefficient
c_{l_μ}	mean section lift coefficient
c_m	section moment coefficient, $c_m \equiv \frac{M_a}{(1/2)\rho_\infty U_\infty^2 c^2}$
C_P	pressure coefficient, $C_P \equiv \frac{p - p\vert_{\tilde{x}/c=0.30}}{(1/2)\rho_\infty U_\infty^2}$
D	section aerodynamic drag force
f	airfoil camber
f_i	objective function
g	gravitational acceleration

[*] Aerospace Engineer, Aeromechanics Branch, NASA Ames Research Center, AIAA Member.
[†] Aerospace Engineer, Aeromechanics Branch, NASA Ames Research Center.
[‡] Aerospace Engineer, Aeromechanics Branch, NASA Ames Research Center, AIAA Fellow.

$\boldsymbol{G}$	generation (vector of chromosomes)
i, j, k, n	counter
L	section aerodynamic lift force
m	mass
M	Mach number
M_a	section aerodynamic pitch moment
M_{tip}	tip Mach number
N	integer number
$\tilde{n}$	transported amplification factor
N_C	number of chromosomes
N_{crit}	critical amplification factor (envelope)
N_G	number of genes
N_O	number of objectives
P	probability
$\boldsymbol{P_i}$	Bézier curve (vector of control points)
R	rotor radius; rank
r	rotor radial coordinate
$R(0,1)$	random number (between 0 and 1, inclusive)
Re	Reynolds number
Re_c	chord-based Reynolds number
t	airfoil thickness
t_b	airfoil baseline thickness
Tu_∞	free-stream turbulence intensity (%)
u, v, w	velocity components
U_∞	freestream velocity
V_{tip}	tip velocity
x	decision variable (gene)
$\boldsymbol{x}$	chromosome (vector of decision variables, genes)
x, y, z	Cartesian coordinates
y^+	dimensionless wall distance
α	angle of attack
β	parameter controlling perturbation mutations
δ_1	leading-edge angle (of double-edged plate)
δ_2	trailing-edge angle (of double-edged plate)
δ_3	leading-edge slope of camber (of cambered plate)
γ	intermittency
$\tilde{\gamma}$	modified intermittency, $\tilde{\gamma} \equiv \ln \gamma$
ρ_∞	freestream density
τ	limited freestream turbulence intensity; Bézier interval

II. Introduction

The Mars Helicopter will be flying on the NASA Mars 2020 rover mission scheduled to launch in July of 2020.[1] The small, autonomous rotorcraft aims to demonstrate the viability and potential of heavier-than-air vehicles in the Mars atmosphere. The Mars atmosphere poses numerous challenges for heavier-than-air flight. The low atmospheric density results in very low chord-based Reynolds numbers for rotor operation, $Re_c \cong 10^4$. The low density and low Reynolds number reduce the lift force and lift efficiency, respectively, which are only marginally compensated for by a lower gravitational acceleration of around $g = 3.71 \ m/s^2$. The predominantly CO_2 based atmosphere results in a low specific heat ratio and gas constant. Combined with the relatively low average temperature, this results in a decreased speed of sound and hence higher observed Mach numbers over the rotor, further constraining rotor operation in the Mars atmosphere.

The design of the MH features a co-axial rotor with a mass of roughly $m = 1.8 \ kg$ and a $R = 1.21 \ m$ rotor diameter. The rotor design features two counterrotating, hingeless, two-bladed rotors using conventional airfoil shapes.[2] The rotors are spaced apart at approximately 8–9% of the rotor diameter and are designed to operate at speeds up to 2800RPM. The tip speed and tip Mach number during hover in the Martian atmosphere are roughly $V_{tip} = 177 \ m/s$ and $M_{tip} = 0.76$, respectively. The helicopter is mounted on the bottom of the Mars 2020 rover for its journey to Mars. The rover places the helicopter on the ground after touchdown, starting a 30-day flight test campaign of up to five flights of a few hundred meters.

Koning, Johnson, and Allan performed an evaluation of the two-dimensional boundary-layer state for the MH airfoils in hover and concluded that laminar-turbulent transition of the boundary layer is unlikely and the flow will remain predominantly laminar over the rotor in hover.[2] The laminar boundary layer separation for conventional airfoils at low Reynolds numbers results in rapid deterioration of the attainable aerodynamic efficiency of the airfoil and, by extension, rotor. Koning, Johnson, and Grip describe the generation of the improved Mars Helicopter aerodynamic rotor model and correlate against experimental performance results of the Mars Helicopter in Mars atmospheric conditions in the 25-ft-diam Space Simulator at the Jet Propulsion Laboratory (JPL).[3] The various boundary layer states and the effect of transition modeling are also discussed.

Research is performed at the Jet Propulsion Laboratory (JPL) and NASA Ames Research Center to extend the capabilities of the MH and develop the MSH as the next possible step for Martian rotorcraft. The MSH mass is scaled up to the 5 to 20 *kg* range, allowing for a science payload (approximately 0.5 to 2.0 *kg*), and greater range (ranging from 900 *m* to approximately 3000 *m*).[4,5] Key to achieving these targets is careful aerodynamic design of the rotor, and therefore, at first, optimal design of the airfoils.

Efficient airfoils at very low Reynolds numbers are relatively unexplored: their applicability for Earth-based vehicles is mainly limited to small Unmanned Aerial Vehicles (UAV), Micro Aerial Vehicles (MAV), and Nano Aerial Vehicles (NAV). Conventional airfoil shapes are likely not the optimal choice for efficient aerodynamic performance of airfoils at low Reynolds numbers. Work by Carmichael,[6] Lissaman,[7] and Mueller and DeLaurier[8] reviews available low Reynolds number airfoil studies, albeit most Reynolds number ranges considered are higher than that required for the present work. Koning, Romander, and Johnson showed Figure of Merit improvements when using cambered plate airfoils as direct substitute for the Mars Helicopter airfoils.[9] Koning, Romander, and Johnson performed single-objective optimization of plate airfoils for the MSH and found promising performance for plate-type airfoils with a sharp leading edge.[10] The present work extends the analysis to *multi-objective optimization* (MOO), using an evolutionary algorithm to identify optimized unconventional airfoil shapes and design trends.

III. Subcritical Airfoil Performance

Conventional airfoils at high Reynolds numbers usually experience laminar-turbulent transition of the boundary layer, allowing the airfoils to reach relatively high lift-to-drag ratios compared to lower Reynolds numbers. The turbulent boundary layer exhibits irregular fluctuations which result in unsteady small-scale eddying motion that causes a continuous transport of energy from the freestream into the boundary layer. The exchange of momentum due to this turbulent mixing causes

an increase in the shear stress at the wall and the time-averaged value of the velocity components.[11] Therefore, the turbulent boundary layer can overcome a larger adverse pressure gradient and hence is less prone to separation, resulting in improved airfoil performance. Whereas the turbulent shear stresses are higher than those found in the laminar boundary layer and thus increase the friction drag, the prevention of flow separation prevents a large increase in pressure drag, resulting in a reduction in net drag.[12] Laminar-turbulent transition only occurs for airfoils above a critical Reynolds number in the supercritical Reynolds number regime (the term 'critical' is used here as the termination of laminar separation).[13,14]

In the subcritical Reynolds number regime, and around the critical Reynolds number regime, however, the airfoil performance deteriorates. The following section discusses the reasons for the relatively poor performance of conventional airfoils at these Reynolds numbers, the relatively good performance of thin or plate-type airfoils. The various instabilities and the phenomena attributing to the complexity of low Reynolds number aerodynamics are also discussed. The term 'turbulence' is used throughout this paper to indicate 'small-scale chaotic motion', not to be confused with laminar unsteady flows.

A. Conventional Subcritical Airfoil Performance

The aerodynamic performance of conventional airfoils starts to deteriorate below roughly $Re_c = 500,000$.[6,7] With decreasing Reynolds number, the relative strength of the viscous forces increases (compared to the inertial forces), progressively damping disturbances found in the flow and delaying the region of laminar-turbulent transition over the airfoil surface. Consequently, the boundary layer on the airfoil upper surface may remain laminar downstream of the point of pressure recovery.[15] The laminar boundary layer can only support a small adverse pressure gradient without separation[11] and will thus commonly separate at lower Reynolds numbers. This is the primary impediment to low Reynolds number (conventional) airfoil performance[16] and can cause large-scale flow separation on the

airfoil. The net drag is increased due to the pressure drag component caused by the separation, despite a possible reduction in friction drag due to the flow reversal in the region of separated flow.[12] The increased thickness of the boundary layer at lower Reynolds numbers[14] (and the possible separation on the aft section of the airfoil) reduce the lift coefficient, albeit to a lesser extent than the increase in drag coefficient.[13]

McMasters and Henderson[17] provide an overview of airfoil performance over a large Reynolds number range as shown in Fig. 1. Around the Reynolds number range $50,000 < Re_c < 200,000$ a reduction in maximum section lift-to-drag ratio for smooth (conventional) airfoils is observed of around 1.5 orders, attributable to the laminar separation of the boundary layer. Airfoils with increased surface roughness are shown to remain competitive until slightly lower Reynolds numbers.
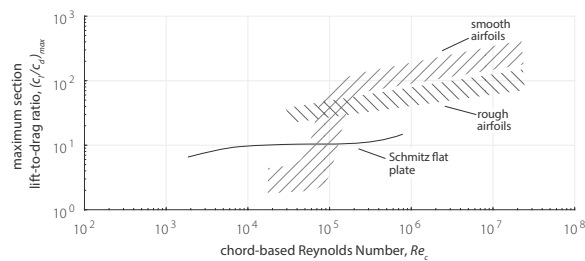
Fig. 1   Lift-to-drag ratio as function of Reynolds number, from McMasters and Henderson.[17]

The minimum section drag coefficient versus Reynolds number for smooth (conventional) airfoils is shown in Fig. 2.
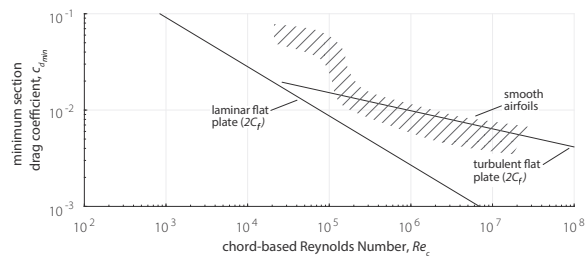

Fig. 2   Minimum section drag as function of Reynolds number, from McMasters and Henderson.[17]

The laminar separated shear layer results in flow destabilization, and the separated shear layer remains detached only at sufficiently low Reynolds numbers (or sufficiently high angles of attack).[6] At slightly higher Reynolds numbers,

the turbulent separated shear layer entrainment causes reattachment of the flow into the turbulent boundary layer on the airfoil further downstream, increasing airfoil performance.[7,18,19] The stability, transition, and unsteady characteristics of boundary layers are fundamentally different from those of separated shear layers.[20] Tollmien-Schlichting (T-S) waves originating from the boundary layer prior to separation are transferred into the laminar separated shear layer and may grow exponentially, possibly causing laminar-turbulent transition of the (separated) shear layer with resulting reattachment.[21,22] The reattachment forms a laminar separation bubble (LSB) and can take the form of a steady, closed separation bubble under a relatively weak adverse pressure gradient.[23] A simplified sketch indicates the flow complexity of an LSB is shown in Fig. 3.
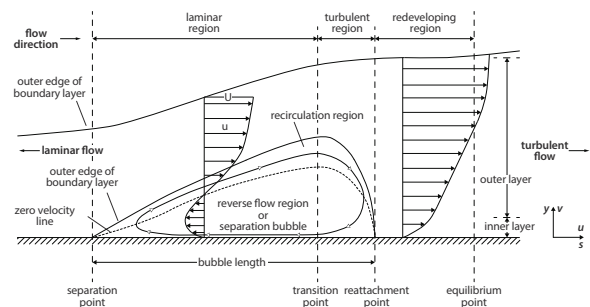

Fig. 3   Elements of a steady (or time-averaged) laminar separation bubble with turbulent reattachment, from Carmichael.[6]

A decrease in T-S wave amplitude can also delay laminar-turbulent transition in the (separated or bounded) shear layer. External disturbances such as freestream turbulence (FST), surface roughness and vibration, and acoustic waves can generate instability waves[20,24] (the process known as receptivity). Therefore, the external disturbances are able to affect the overall amplification of disturbances in the separated shear layer, and hence change the location of turbulent reattachment. Freestream turbulence effects on separation bubble properties and low Reynolds number performance were shown experimentally by O'Meara and Mueller, Simoni et al.,[25] Laitone,[26] and Wang et al.[27] The reverse flow region in the separation bubble can also cause the laminar region of the bubble to be affected by backward effects from the disturbed

flow in the downstream part of the bubble.[21] The overall T-S wave amplitude is difficult to predict because the contributors to shear layer receptivity are inherently difficult to accurately model, and can behave highly nonlinear. As amplification is also dependent on the correct frequency band, the analysis is complicated further and might cause difficulty correlating experiments to simulations.[28]
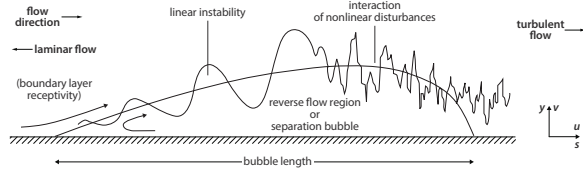

Fig. 4   Aspects of laminar flow breakdown in the separation region, from Boiko et al.[21]

The transition to turbulence in the separated shear layer and subsequent reattachment of the turbulent boundary layer is one of the phenomena that occur at laminar flow destabilization. The instability to T-S waves is often the primary instability up to the separated flow region, whereas the separated shear layer is subsequently also unstable to the Kelvin-Helmholtz (K-H) instability.[29–32] The shedding of coherent vortices is often accredited to the primary instability mechanics of the K-H instability[23] and may have a large impact on the fluctuating forces on the airfoil.[33]

Increasing strength of the adverse pressure gradient causes progressive undulation of the separated shear layer and oscillation of the reattachment location. The oscillation due to the (inviscid) K-H instability can cause the shear layer to 'roll-up' as a prelude to the onset of K-H vortices which can develop downstream, amalgamate, and ultimately cause the formation of large-scale vortex shedding.[21,25,29,33,34] The vortex roll-up of the separated shear layer due to the K-H instability is sketched in Fig. 5. The shear layer velocity profile can be decomposed into a constant and equal velocity across the shear layer and a velocity shear component. The velocity shear component results in pressure differences that start the K-H instability and ultimately cause vortex formation.

Gaster[35] first observed 'bubble bursting' which is the process through which a 'short bubble'

transitions to a 'long bubble'. This is likely the transition from a steady to a (time-averaged) unsteady LSB and indicates the onset of vortex shedding, as reported by Pauley, Moin, and Reynolds.[29] The shedding of large-scale vortical structures is not caused by laminar-turbulent transition upstream, but can initiate transition, promote turbulence, and contribute to (possible) boundary layer reattachment.[25,29] As the Reynolds number is decreased, the wavelength of the K-H vortices is seen to increase.[34] At higher angle of attack, or at increased strength of the adverse pressure gradient, the shear layer oscillations occur earlier and stronger with larger observed K-H vortices.[33]
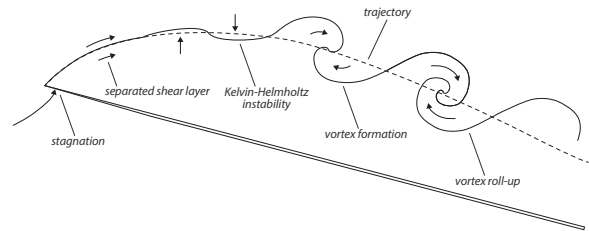

Fig. 5   Schematic representation of vortex roll-up due to the Kelvin-Helmholtz instability of a separated shear layer.

The range $30{,}000 \stackrel{<}{\sim} Re_c \stackrel{<}{\sim} 70{,}000$ is of interest to MAVs[8] or small UAVs[27] and can hence make use of the findings in the present work. Below $Re_c \cong 50{,}000$ the laminar separated shear layer on a (conventional) airfoil normally does not transition to turbulent flow in time to reattach to the airfoil surface.[6,8] The primary chord-based Reynolds number range of interest for a Mars rotor airfoil is around $10{,}000 < Re_c < 30{,}000$.[2,3,10] The instabilities of the separated flow, both transition to turbulence and self-excited shedding of coherent vortices, have a strong impact on airfoil operation and stall at low Reynolds numbers. Wang et al. investigated the NACA 0012 airfoil at chord-based Reynolds numbers between $5{,}300 < Re_c < 20{,}000$ with varying turbulence intensity of the oncoming flow.[27] The analysis describes eight distinct flow structures in four proposed Reynolds number regimes, as shown in Fig. 6.

The flow structures identified by Wang et al. in Fig. 6 are flow structure A, *"a fully attached laminar boundary layer"* at sufficiently low Reynolds number, flow structure B, *"a partially*

attached laminar boundary layer with separation near the trailing edge without reattachment of the flow", flow structure C, *"a fully separated laminar boundary layer without reattachment of the flow"*, flow structure D, *"a laminar bubble with possible transition downstream"*, and flow structure E, *"laminar separation with turbulent reattachment."*[27]
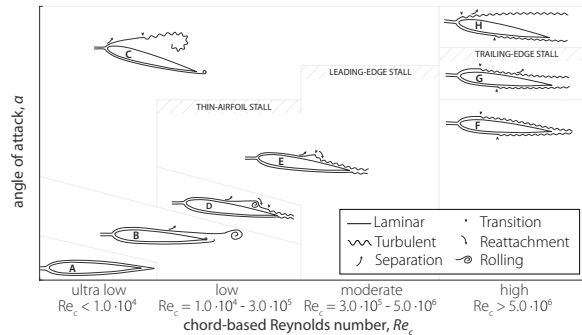

Fig. 6   Schematic of flow structures around NACA 0012 airfoil for each Reynolds number regime, from Wang et al.[27]

Koning, Johnson, and Grip generated an aerodynamic rotor model for the NASA Mars Helicopter using two-dimensional time-accurate CFD simulations in OVERFLOW for comprehensive analyses. They correlated the observed flow structures over the (conventional) outboard airfoils at various angles of attack to flow structures B, C, and D.[3] As angle of attack or Reynolds number[26] is varied, the flow state can switch between structures A to E; leading to pre-stall nonlinearity in the lift curve as experimentally observed by Wang et al.[27] Largely laminar behavior of the bounded and separated shear layer was observed with possible exceptions at high angles of attack and/or higher Mach numbers. Koning, Johnson, and Allan applied a simplified linear stability theory (LST) model to the boundary layer of the (conventional) airfoils of the NASA Mars Helicopter.[2] T-S waves were assumed to be the dominant transition-initiating mechanism and steady boundary layers in predominantly two-dimensional flow were assumed. It was concluded from the cumulative amplification ratio over the airfoil and boundary layer Reynolds numbers upon separation that transition of the boundary layer is unlikely and the flow will remain predominantly laminar over the MH rotor in hover.

Huang and Lin also studied the flow patterns and unsteady flow structures on a NACA 0012 as shown in Fig. 7. The region between the dashed lines indicate the Reynolds number region that could not be identified due to experimental difficulties. The findings are in overall agreement with the work from Wang et al.[27] They further analyze the von Kármán vortex street in the wake of the airfoil and observe fully laminar behavior at the low end of the investigated Reynolds number range.[36]
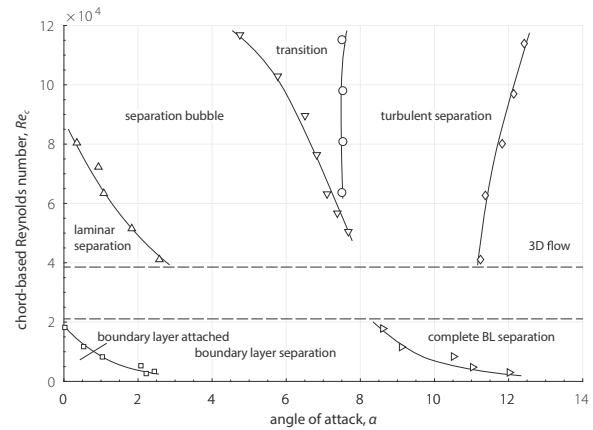

Fig. 7   Regions of characteristic flow modes of an NACA 0012, from Huang et al.[36]

The work from Wang et al.[27] and Huang and Lin[36] indicates that the NACA 0012 airfoil under low angles of attack and $Re_c \gtrsim 50{,}000$ experiences laminar separation without reattachment and causes severe deterioration of the airfoils' aerodynamic performance. Wang et al. attribute the deterioration of airfoil performance in the low and ultra-low Reynolds number range to this behavior. Yarusevych and Sullivan[37] investigate the NACA 0025 airfoil and observe turbulent reattachment of the separated shear layer at $Re_c = 150{,}000$. At lower Reynolds numbers, $Re_c = 55{,}000$ and $Re_c = 100{,}000$, the K-H vortices in the shear layer propagate further downstream without turbulent reattachment. Carmichael estimates a chord-based Reynolds number of $Re_c < 50{,}000$ for the occurrence of reattachment after laminar separation in a non-turbulent stream for conventional airfoils.[6]

Slightly higher Reynolds numbers are more prone to separation bubbles, increasing

performance compared to laminar separation without reattachment. The performance remains hard to reliably predict, as the freestream turbulence level can have a dramatic effect on the LSB behavior, and thereby airfoil performance. Variations in freestream turbulence levels in experiments at low Reynolds numbers have shown large performance changes. Hoffmann observed a 30% increase of $c_{l_{max}}$ for a NACA 0015 at $Re_c = 250,000$[38] and Laitone shows a 49% decrease in lift-to-drag ratio for a NACA 0012 airfoil at $Re_c = 20,700$ with varying FST levels.[26] Wang et al. observe $c_{l_{max}}$ and c_l/c_d are increased by 52% and 454%, respectively, at $Re_c = 5,300$, and $c_{l_{max}}$ changes by 10% around $Re_c = 20,000$ for the NACA 0012 airfoil with varying levels of FST.[27] Turbulence intensity changes show similar effects on airfoil performance as changes in chord-based Reynolds number.[27] As such, it is hypothesized that any other parameter influencing the receptivity of the boundary layer (surface roughness, vibrations, and acoustic waves) can cause similar fluctuations in measured or predicted airfoil performance.

B. Sharp Leading Edge Performance at Low Reynolds Numbers

Around and below $Re_c = 50,000$ a conventional airfoil shape is a suboptimal choice to achieve good aerodynamic performance.[6,8,39] The primary reasons for this are (i) laminar separation without reattachment at the lower Reynolds number bound will result in high pressure drag and reduced lift and (ii) the Reynolds number, and factors influencing the receptivity of the boundary layer, can make airfoil performance highly dependent on flow and airfoil conditions.

It has been observed that flat and cambered plates in this Reynolds number range provide relatively high aerodynamic performance. Hoerner compares the performance of the N60 (conventional) airfoil to a cambered plate between $10,000 < Re_c < 1,000,000$ and shows the dramatic performance drop of the conventional airfoil as it enters the subcritical regime. This is in comparison to the relatively constant performance of the cambered plate.[13] The section lift and drag versus Reynolds number are shown

in Fig. 8 and Fig. 9, respectively. The relative increase of the performance of a flat plate can also be seen in Fig. 1, simple flat plates outperform conventional airfoil sections for $Re_c \gtrsim 80,000$.[13,17,26]
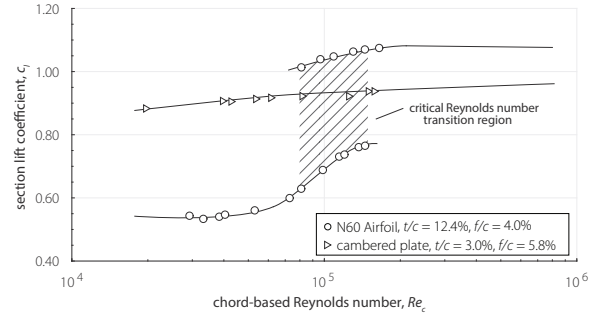

Fig. 8   Section lift coefficient versus Reynolds number at constant angle of attack, from Hoerner.[13]
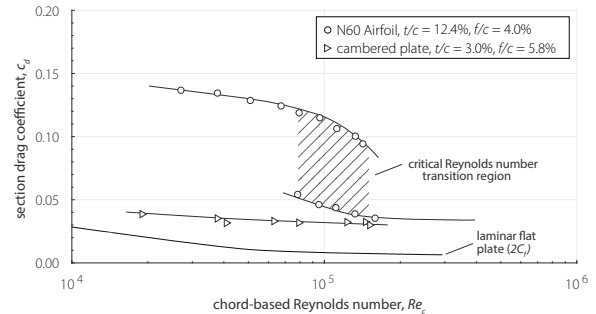

Fig. 9   Section drag coefficient versus Reynolds number at constant angle of attack, from Hoerner.[13]

Circular arc airfoils with a camber value of around 5% are observed to outperform conventional airfoils and flat plates.[13,14,17,26,40] Schmitz[14] performed pioneering work in characterizing the performance of (cambered) plates at low Reynolds numbers. Schmitz attributes the superiority of a thin, cambered airfoil under $Re_c = 100,000$ to '*favorable interaction of tangential approach flow to the leading edge at large angles of attack and nose turbulence*,' '*the large camber of the lower surface*,' and '*the relatively small curvature of the rearward upper surface*.'[14] As the latter two arguments for the high performance can be present in a thin conventional airfoil as well, the primary focus will be placed on the sharp leading edge. The most striking example of the added performance due to the sharp leading edge might be the performance increase of the reversed NACA 0012 airfoil at low Reynolds numbers

(trailing edge pointing upstream), indicating the importance of this feature to the performance at lower Reynolds numbers.[41,42]

Koning, Romander, and Johnson analyze a cambered plate and a flat plate as a direct substitute for the NASA Mars Helicopter rotor in hover and find an increase in rotor Figure of Merit throughout the thrust coefficient range for the cambered plate. A 7% increase in maximum rotor thrust and a 5% increase in rotor Figure of Merit over the design coefficient range are observed compared to the NASA Mars Helicopter.[9]

Sharp leading edges induce a high adverse pressure gradient at the leading edge, enforcing flow separation at the leading edge and promoting the shedding of vortices.[21,43] The shed vortices can mitigate total flow separation[26] and the separated shear layer can rapidly undergo laminar-turbulent transition due to increased entrainment facilitating upper surface turbulent reattachment of the boundary layer in the form of an (unsteady) long separation bubble.[13,33,39,44] As mentioned earlier the separated shear layer is subsequently also unstable to the Kelvin-Helmholtz (K-H) instability,[29–32] promoting the shedding of coherent vortices. K-H vortices can have a large impact on airfoil performance, and with increasing strength of the adverse pressure gradient the shear layer oscillations can start further upstream, and produce stronger and larger K-H vortices.[33]

Koning, Romander, and Johnson performed optimization of plate airfoils with sharp leading edges at low Reynolds numbers. Amongst others, a plate with a cubic variation of its camber line and a double-edged plate airfoil (see Fig. 21) were investigated.[10] Single objective optimization at target $c_l \cong 0.65$ for $M = 0.30$ and $M = 0.50$ showed the shedding of vortices over the upper surface for all optimized geometries and conditions. Lift-to-drag increases for the double-edged plate are around 7% to 12% and 15% to 28%, compared to the cambered plate or Mars Helicopter outboard (conventional) airfoil, respectively. Recently, Traub and Coffman also show the improvements of a flat plate with deflected leading and trailing edge flaps compared with a circular arc airfoil and three conventional airfoils with average lift-to-drag ratio increase of

14% around $40{,}000 <= Re_c <= 80{,}000$. Besides plate airfoils, other sharp leading edge airfoil geometries are investigated such as a triangular airfoil (see Fig. 13) by Munday et al.[45] and polygonal airfoils by Koning et al.[10]

Okamoto et al.,[46] Laitone,[26] and Pelletier and Mueller,[47] show the comparatively low influence of freestream turbulence to plate performance.

For Mars rotor applications a relatively high Mach number is observed due to the low speed of sound in the Mars atmosphere (based on the lower values of the specific heat ratio, gas constant, and temperature in the Mars atmosphere). Anyoji et al.[48,49] conclude that flat plates are relatively insensitive to Mach number at $4{,}300 <= Re_c <= 41{,}000$ and $0.1 <= M <= 0.6$.[48] In addition, Anyoji et al.[49] show that the specific heat ratio in the Mars atmosphere has little effect on the aerodynamic performance. Suwa et al.[50] also show the relative Mach number insensitivity of sharp leading edge airfoils at $Re_c = 3{,}000$ and $Re_c = 10{,}000$ for $M = 0.15, 0.50$, and 0.70. Chapman, Kuehn, and Larson[51] investigate transition of separated flows at higher Mach numbers behind sharp edges and observe increased stability of the laminar separated shear layer with Mach number.

C. Laminar-Turbulent Transition and Shedding Instabilities

At low chord-based Reynolds numbers fully laminar separation bubbles (with or without transition *downstream* of the reattachment location) over airfoils can occur[51–53] and have been observed experimentally.[27,36,48] Also the separation bubble behind a flat plate at $\alpha = 2.5°$ at $Re_c = 10{,}000$ is observed to have laminar reattachment.[54,55] Often, laminar-turbulent transition of the free shear layer is the sole reason mentioned for reattachment of the boundary layer, similar to the sketch shown in Fig. 4. This is likely due to the higher Reynolds number range discussed in the majority of low Reynolds number research, focusing around $Re_c \cong 10^5$, where this can be the dominant instability. However, other instability phenomena are initiated by the separated shear layer resulting in large-scale two- and three-dimensional vortices shedding into the reattached boundary layer.[43] The absence of steady separation bubbles (versus large-scale

unsteady vortex shedding) results in an absence of stall, in the sense of a steep drop in lift coefficient or steep rise in section drag coefficient.[56]

The vortices can be generated through growth of the separated shear layer disturbances,[43] K-H instabilities,[25,30,33] or possibly different shedding type instabilities.[52] Boiko et al. note that the influence of laminar-turbulent transition is marginal compared to the instability phenomena initiated by the separation and that they occur independently from each other.[43] Pauley, Moin, and Reynolds also conclude that unsteady separation arises from the separated shear layer instability and that the large coherent vortices play a dominant role in the (unsteady) reattachment over the small-scale turbulence.[29] The periodic vortices are thus not produced by amplification of the shear layer disturbances but are hypothesized to be self-excited systems influenced only by local stability properties.[43] That the instabilities are only marginally influenced by small-scale chaotic motion (turbulent flow) is crucial in explaining the relatively good performance of sharp leading edge airfoils: the high adverse pressure gradient promotes the shedding of coherent vortices, that mitigate the effect of total flow separation, independent of laminar-turbulent transition. The contribution of the vortices to the separated flow still depends on the flow configurations, the mean parameters, and environmental perturbations.[21] Downstream of the onset of shedding, neighboring vortices can amalgamate and transform into two- and three-dimensional structures, ultimately breaking down to turbulent flow.[25,30,33,57] However, the contributions of laminar-turbulent transition after an initial laminar shedding process is hypothesized to be secondary to the 'certainty' of vortex shedding in the Reynolds number range under consideration for airfoils with sharp leading edges. At lower Reynolds numbers, however, the K-H vortices do not have to break down and can propagate further downstream and influence the wake vortex shedding characteristics.[31] The leading edge shear layer and possible K-H vortices will interact with Karman vortices shed at the trailing edge, further influencing airfoil performance.[33]

The Reynolds number range of interest here is close to that studied for biological sources for insect and bird flight. Dragonfly airfoils studied in steady flow below $Re_c = 8,000$ are found to operate in laminar flow,[58] despite the large corrugations present along the chord. Swift airfoils contain leading-edge corrugations up to 5-10 times smaller in amplitude compared to dragonfly wings,[59–61] and a height of around 2% chord (similar to the measured local boundary layer), but the flow is observed to remain laminar for lower angles of attack at $Re_c = 13,300$ and $\alpha = 4.5°$.[61,62] Hummingbirds wings in steady flow have been observed to not operate in fully laminar flow between $5,000 < Re_c < 15,000$ at a higher angle of attack, $\alpha = 10.0°$.[63]

The mitigation of large-scale flow separation by the leading-edge shedding of coherent vortices (in absence of the performance degradation due to a laminar separation without reattachment) is the primary reason for the relatively good performance of sharp leading edges around $Re_c = 50,000$ and below. This is in sharp contrast to conventional airfoil performance where the onset of large-scale vortex shedding (or 'bubble bursting') and collapse of the laminar separation bubble marks the onset of poor performance (compared to laminar-turbulent transition and boundary layer reattachment).[27] The shear layer instabilities resulting in the onset of vortex shedding are separate from laminar-turbulent instabilities and therefore, can prove reliable at these and perhaps lower Reynolds numbers. On top of that, the relatively low influence of freestream turbulence values, and assumed other possible receptivity processes, reduce the sensitivity to operating conditions that is common for conventional airfoils around this Reynolds number range.

IV. Evolutionary Multi-Objective Optimization

Numerous strategies exist to address multi-objective optimization (MOO) problems. The present work uses Evolutionary Multi-Objective Optimization (EMOO). There exist numerous EMOO techniques with their own advantages and disadvantages; an overview can be found in the

work by Coello.[64] The present work is the continuation of a previous study focusing on optimization of plate airfoils for Martian rotor applications using single-objective optimization (SOO) by Koning et al.[10] Here, an EMOO approach similar to the Nondominated Sorting Genetic Algorithm[65,66] (NSGA) and the Multi-Objective Genetic Algorithm (MOGA)[67] is used and follows the approach as presented by Holst and Pulliam.[68] The main advantages for using MOGA optimization are the relatively simple implementation, the parallel nature of the procedure, and the robustness of the approach, as it does not rely on a smooth unimodal design space (no derivative information is required).[69,70] It is assumed that the unconventional airfoils under consideration are prone to result in multiple local optima in the design space in the current (or potential future) studies. A downside of the MOGA approach is expense, as in general more function evaluations are required when compared to gradient-based methods.[68,69]

In MOO it is uncommon for a single optimal solution to exist with respect to all objectives. MOO techniques therefore give rise to a set of Pareto optimal solutions instead of a single design solution that is usually obtained using SOO methods. A vector of decision variables is Pareto optimal if *no improvement can be achieved in one cost vector component that does not lead to degradation in at least one of the remaining components.*[67] The multi-objective problem is of the form:

$$\text{minimize} \left(f_1(\boldsymbol{x}), \dots, f_k(\boldsymbol{x}), \dots, f_{N_O}(\boldsymbol{x}) \right)$$

where N_O is the number of objective (cost) functions f_i that are to be minimized and $\boldsymbol{x}$ is the decision variables vector. A decision variable vector $\boldsymbol{x}^* = \left(x_1, \dots, x_i, \dots, x_{N_G} \right)$ in the design space Ω that satisfies all constraints is Pareto optimal if there is no other $\boldsymbol{x} \in \Omega$ such that $f_i(\boldsymbol{x}) \leq f_i(\boldsymbol{x}^*)$ for all $i = 1, \dots, N_O$ and $f_j(\boldsymbol{x}) < f_j(\boldsymbol{x}^*)$ for at least one j. The final solution is the set of Pareto optimal points or the Pareto optimal set. All vectors of decision variables in the Pareto optimal set are called *nondominated*, or *noninferior*. The Pareto optimal set allows for the direct evaluation of the decision variable variation without choosing weighting factors prior to knowing their influence.

A. Genetic Algorithm

The Genetic Algorithm is the driver of the MOGA approach, and combines ranking and selection techniques in combination with a variety of modification operators to balance exploitation and exploration of the solution space. A Continuous Genetic Algorithm (CGA) is used in the present studies instead of binary-encoding, as this is shown to reduce computational expense[71] and describes the decision variables more logically.[68] The optimization procedure as described by Holst and Pulliam[68] is used for the present work, with only minor variations. For the benefit of the reader, certain parts of the procedure and the modification operators as presented by Holst and Pulliam are repeated here for clarity; and the reader is referred to the reference for a more in-depth description.[68]

In GA jargon a *population* consists of multiple decision variable vectors $\boldsymbol{x}$, or *chromosomes*, which in turn consist of n design variables x, or *genes*. A chromosome contains the complete specifications of a possible design and is described by

$$\boldsymbol{x}_j^n = \boldsymbol{x}_j^n \left(x_{1,j}^n, \dots, x_{i,j}^n, \dots, x_{N_G,j}^n \right)$$

where $\boldsymbol{x}_j^n$ is chromosome number j of the population, which corresponds to generation number n. Each chromosome consists of N_G genes $x_{i,j}^n$ with gene number i.

Each gene is subject to (in)equality constraints which limit the airfoil geometry so as to limit the design space to reasonable airfoil geometries in terms of, for example, camber and slope constraints.

1. Initialization
The initial generation $\boldsymbol{G}^n = \boldsymbol{G}^0$ is formed using a (constant) population size $N_C = 20$

$$\boldsymbol{G}^0 = \left(\boldsymbol{x}_1^0, \dots, \boldsymbol{x}_j^0, \dots, \boldsymbol{x}_{N_C}^0 \right)$$

and each gene within each chromosome $\boldsymbol{x}_j^0$ is initialized, where possible, using

$$x_i = R(0,1)(x_{max_i} - x_{min_i}) + x_{min_i}$$

with $R(0,1)$, a random numerical value between 0.0 and 1.0, inclusive. Certain constraints, such as minimum enclosed angle limitations for correct meshing, or slope limitations on a Bézier curve element, are dependent on multiple genes, or are hard (or impossible) to explicitly encode in some cases. In these cases, the constraints are enforced implicitly while efforts are taken to minimize the influence on the workings of the GA itself. The coupling between different parameters of an objective function, or *epistasis*, cannot become too high as this will negatively impact the GA performance.[72]

2. Ranking

The flow solver OVERFLOW 2.2o[73] is used to evaluate the cost (or fitness) of each chromosome, as will be discussed in the following chapters. Representative objective functions could be the minimization of drag and the maximization of lift. After the cost is assigned for all objective functions, all chromosomes in the population are given a rank using Goldberg ranking.[74]

The algorithm starts by identifying all nondominated chromosomes of the population and assigns them rank $R = 1$, after which the chromosomes are removed from the population. The nondominated chromosomes of the remaining population are given rank $R = 2$. This process continues until all chromosomes are given a rank. The rank 1 chromosomes of the population are then ranked against the rank 1 chromosomes of the previous generation, resulting in a Pareto optimal set for the current generation.

3. Selection

The distance between Pareto optimal solutions in objective space is used to sort the chromosomes prior to extracting the top N_C chromosomes for modification operators, increasing the selection chances for nondominated chromosomes in underdeveloped regions of the Pareto front in an effort to distribute the solutions over the front. The Pareto end points are always included in the selection as the top chromosomes to avoid local refinement of the Pareto front. This selection procedure bears resemblance to the *bin selection* as described by Holst and Pulliam[68] and the uniqueness value in the NSGA algorithm. The final selection is placed in the selection array

$$\boldsymbol{G}^t = (\boldsymbol{x}_1^t, \dots, \boldsymbol{x}_j^t, \dots, \boldsymbol{x}_{N_C}^t)$$

If the Pareto optimal set for the current generation contains less rank 1 chromosomes than the population size N_C, the selection adds the highest ranking chromosomes to the selection until the number of chromosomes matches N_C.

4. Modification Operators

After the selection of chromosomes $\boldsymbol{G}^t$ has been made, various modification operators are applied to create the next generation of chromosomes. For clarity to the reader, the modification operators as presented by Holst and Pulliam are repeated here; and the reader is referred to the reference for a more in-depth description.[68]

Passthrough

The first 10% (or 2 chromosomes with the $N_C = 20$) from $\boldsymbol{G}^t$ are passed through to the next generation without any modification. These are always the chromosomes with the highest individual fitness (i.e. the Pareto front end points), guaranteeing that maximum individual fitness will never drop between generations.

Random Average Crossover

The following 30% (or 6 chromosomes with the $N_C = 20$) of the next generation consists of chromosomes obtained using random average crossover. For each randomly-chosen chromosome in the next generation, two chromosomes $\boldsymbol{x}_{j1}^t$ and $\boldsymbol{x}_{j2}^t$ are randomly chosen from the selection $\boldsymbol{G}^t$ and form a new chromosome by combining part of the gene values from each

$$x_{i,j}^{n+1} = 0.5(x_{i,j1}^t + x_{i,j2}^t) \; i = 1,2,\dots,N_G$$

where $x_{i,j}^{n+1}$ is gene i of chromosome j for generation $n+1$ and $x_{i,j1}^t$ and $x_{i,j2}^t$ are the gene numbers i, from chromosomes $\boldsymbol{x}_{j1}^t$ and $\boldsymbol{x}_{j2}^t$, respectively.

Perturbation Mutation

The following 30% of the next generation consists of chromosomes obtained using the perturbation mutation operator. For each randomly-chosen chromosome in the next generation, each gene has a probability of $P = 0.5$ to be perturbed a slight amount according to the following formula

$$x_{i,j}^{n+1} = x_{i,j}^t + (x_{max_i} - x_{min_i})[R(0,1) - 0.5]\beta$$

where $\beta = 0.10$ controls the size of the perturbation mutation and $R(0,1)$ is a random numerical value between 0.0 and 1.0, inclusive. The resulting value of each gene that is perturbed is checked against the constraints and modified if necessary.

Mutation

The last 30% of the next generation consists of chromosomes obtained using the mutation operator. This method operates similarly to the perturbation mutation operator with the difference being that each gene value is randomly chosen between the allowed constraints instead of just being perturbed. For each randomly-chosen chromosome in the next generation, each gene has a probability of $P = 0.5$ to be perturbed according to the following formula

$$x_{i,j}^{n+1} = (x_{max_i} - x_{min_i})R(0,1) + x_{min_i}$$

More details on the implementation of these operators can be found in the work by Holst and Pulliam.[68,75] The gene-space transformation is not used in the present work.

B. Design Space

Two airfoil types are investigated for the present work: a cambered plate with a cubic Bézier curve as camber line and a double-edged plate type airfoil. As the application for the airfoils is targeted at moderate to high subsonic Mach numbers, the thickness is kept low ($t/c = 0.01$). Prior work using SOO methods[10] showed that including thickness variation still resulted in thin airfoils, despite the much longer time needed for convergence due to the added design variables.

Both airfoil types have a thickness of $t/c = 0.01$ and a sharp leading edge. The bevel on the leading each is slightly rounded to avoid an infinitely sharp leading edge. Optimized designs might be possible where the leading edge is too thin for a realistic (manufacturable) design. It is assumed, however, that a blunter leading edge with low thickness will have minimal effects on the aerodynamic performance, similar to the airfoils examined by Traub and Coffman.[39] Both airfoils contain two control points to define the geometry (each with two design variables), and angle of attack as the fifth design variable. Constraints are applied to ensure that practically all gene combinations yield airfoils with realizable geometry. The geometry definition for these airfoils is identical to previous work,[10] but is repeated here for the benefit of the reader.

1. Cambered Plate (CP)

Curved distributions of camber or thickness are parameterized using cubic Bézier curves. The cubic Bézier curve takes shape in the following form

$$\boldsymbol{B}(\tau) = (1-\tau)^3\boldsymbol{P}_o + 3(1-\tau)^2\tau\boldsymbol{P}_1 + 3(1-\tau)\tau^2\boldsymbol{P}_2 + \tau^3\boldsymbol{P}_3$$

where τ is the Bézier interval ranging from $\tau = 0$ to $\tau = 1$, $\boldsymbol{P}_i = [x,y]$ are vectors containing the control points (with $i = 1,...,3$) and $\boldsymbol{B}(\tau) = [x,y]$ is the point on the Bézier curve for the chosen value of the Bézier interval, τ.

The control points are constrained so that x is monotonic in τ, and correspondingly, for each x value there can only be one y value. Cubic Bézier curves can have one or two inflection points, a cusp, be a plain curve, or can contain a loop. Stone and DeRose analyze planar parametric cubic curves and determine the conditions for loops, cusps, and inflection points.[76] The approach by Stone and DeRose is used to ensure constraints enforce the absence of loops as they result in impossible airfoil geometry. Inflection points and cusps are allowed.

A circular arc type airfoil was shown to be aerodynamically efficient[14,26,42,46] and, although a cubic Bézier curve cannot exactly replicate a circular arc, the closest approximation results in

negligible deviation of the camber line from the exact solution.[10]

Table 1 shows the base constraints for the double-edged plate geometry, and Table 2 shows the chromosome buildup.

Table 1 Basic constraints for cambered plate airfoil

Constraint	Minimum	Maximum
Camber slope	-0.50	0.50
Camber height (y/c)	-0.10	0.10
Baseline thickness (t/c)	0.01	0.01
Angle of attack, α	-2.50	7.50

Table 2 Design variable vector for cambered plate airfoil

Decision variable/Gene	Parameter
1	Camber cubic Bézier control point 1, x
2	Camber cubic Bézier control point 1, y
3	Camber cubic Bézier control point 2, x
4	Camber cubic Bézier control point 2, y
5	Angle of attack, α

The cubic Bézier curve representing the camber line, the airfoil thickness distribution, and the final airfoil shape is shown in Fig. 10.
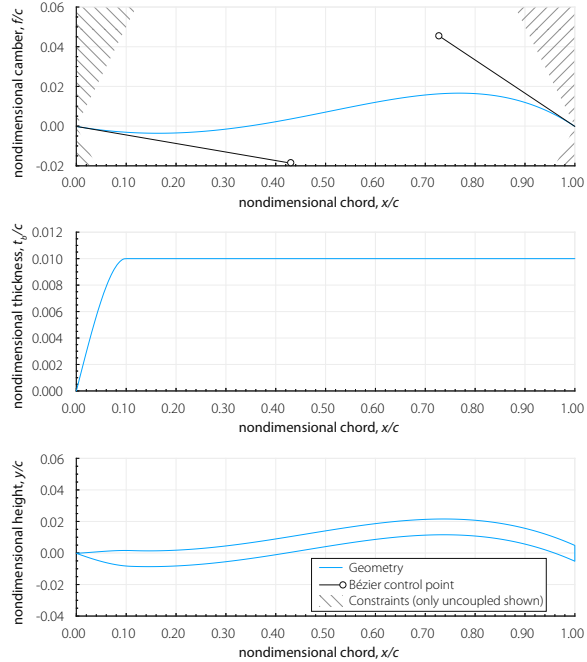
Fig. 10 Cambered plate camber, baseline thickness, and airfoil shape. The vertical axis is enlarged to show details.

The CP airfoils have a fixed thickness distribution and the plate has a thickness of $t/c = 0.01$ to allow a structurally realistic design. The sharp leading edge blends smoothly with the constant thickness plate over the first 10% of the chord. The trailing edge is blunt with a thickness of $t/c = 0.01$. To avoid infinitely sharp edges, elliptic smoothing is applied to the leading edge of the airfoil. The camber control points are visualized with black circles and are constrained to not let the leading and trailing edge slopes exceed the constraints. The maximum slope of the curve and camber height is also constrained.

2. Double-edged Plate (DEP)

To evaluate faceted edges against smooth shapes, a double-edged plate is proposed, as shown in Fig. 11. Two camber control points are allowed to vary within constraints. A linear baseline thickness of $t/c = 0.01$ at the x-coordinates of the two control points is added.
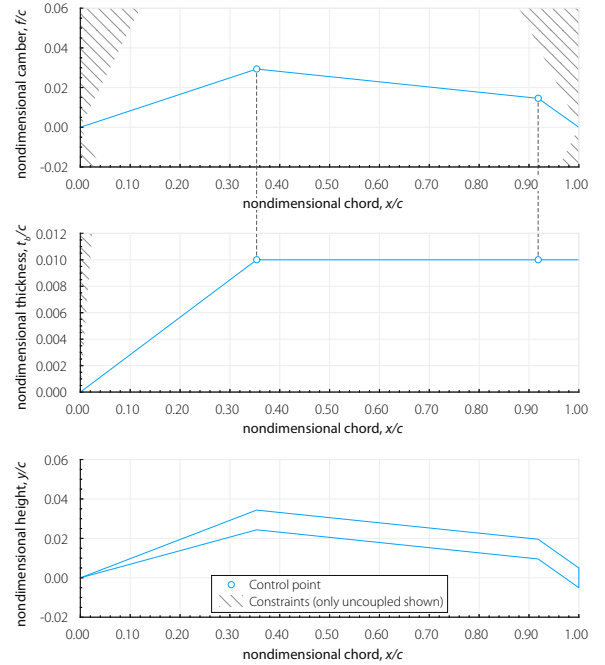
Fig. 11 Double-edged plate camber, baseline thickness, and airfoil shape. The vertical axis is enlarged to show details.

To ensure proper gridding, the smallest enclosed angle between two line segments at a control point is constrained to 130 degrees in the present work. The second control point cannot lie on an x-coordinate smaller than the first control point. For high subsonic Mach numbers, the first x-coordinate is constrained to lie in the first 50% of the chord, as the optimizer could push to create a very thin wedge shape.

Table 3 shows the base constraints for the double-edged plate geometry, and Table 4 shows the chromosome buildup. To avoid infinitely

sharp edges, elliptic smoothing is applied to both the leading edge and upper surface edges of the airfoil.

Table 3 Basic constraints for double-edged plate airfoil

Constraint	Minimum	Maximum
Camber slope	-0.50	0.50
Camber height (y/c)	-0.10	0.10
Baseline thickness (t/c)	0.01	0.01
Angle of attack, α	-2.50	7.50

Table 4 Design variable vector for double-edged plate airfoil

Decision variable/Gene	Parameter
1	Camber control point 1, x
2	Camber control point 1, y
3	Camber control point 2, x
4	Camber control point 2, y
5	Angle of attack, α

V. Objective Space: Computational Fluid Dynamics Approach

Optimization of two-dimensional airfoils at low Reynolds number and high subsonic Mach number while minimizing drag and maximizing lift is performed. Lift and drag values for all airfoils are obtained using the Reynolds-Averaged Navier-Stokes (RANS) solver OVERFLOW 2.2o[73] and used in the fitness functions evaluation. In case of oscillatory flow in the converged solution, Fourier techniques are used to extract mean values.

The numerical approach is, to a large extent, similar to that used by Koning et al. for single objective optimization.[10] Certain elements are repeated for the benefit of the reader. A grid resolution study for the present work is impractical due to the large number of geometries the optimization evaluates. Instead, two representative validation cases are presented for a triangular airfoil at $Re_c = 3{,}000$ for $M = 0.15$ and $M = 0.50$, and a flat plate with leading and trailing edge flaps at $Re_c = 40{,}000$ at low Mach number. The influence of the use of a transition model is also compared with fully laminar calculations at various representative Reynolds-Mach number combinations.

A. Reynolds-Averaged Navier-Stokes Approach Using OVERFLOW

All airfoils are analyzed using two-dimensional structured grids and solved using the implicit, compressible Reynolds-Averaged Navier-Stokes (RANS) solver OVERFLOW 2.2o.[73] For the low Reynolds numbers under consideration the flowfield can be either laminar or transitional, which can benefit from the use of a transition model[77] instead of a 'fully turbulent' RANS simulation; this is because most turbulence models are not designed to predict transition. Transition modeling, when employed, is realized using the Spalart-Allmaras (SA) 1-equation turbulence model[78] (SA-neg-1a) with the Coder 2-equation Amplification Factor Transport (AFT) transition model (SA-AFT2017b).[79] The SA-AFT2017b model will be referred to as the 'transition model' from here on out. All solutions presented are run time-accurate, in an effort to quantify possible unsteady behavior, and use 6th order central differencing of the Euler terms with 2nd order BDF2 time marching.[73]

The function evaluation using a RANS-approach is costly for optimization compared to mid-fidelity methods such as XFOIL.[80] A RANS-based method is a minimum requirement to evaluate the flow physics and airfoil performance for the present work as immediate leading-edge separation, unsteady boundary layers, and high subsonic Mach numbers are of interest. It is assumed that the optimized airfoils will all be in a pre-stalled condition, as the performance evaluation of airfoils with complete flow separation is difficult. Unless noted otherwise, all optimization is performed for representative Mars atmospheric conditions, as found in Koning et al.[3] The parallel nature of the Genetic Algorithm (GA) is used by running all chromosomes in parallel on the Pleiades supercomputer at NASA Ames Research Center, which partly offsets the expense (in time at least) of the GA approach.

1. Fitness Function

The fitness function is the subroutine that assigns the value (cost or fitness) to a set of variables (section lift and drag in this case). The algorithm is set up to minimize all objectives, so the fitness function is set to

$$f_1 = \left(1 - \frac{c_{l_\mu}}{c_l^*}\right)^2 \quad f_2 = \left(1 - \frac{c_d^*}{c_{d_\mu}}\right)^2$$

where c_l^* is a high (unattainable) reference lift coefficient $c_l^* = 2.00$ and c_d^* is a low (unattainable) reference drag coefficient $c_d^* = 0.01$. If a solution diverges, or if a negative lift coefficient is obtained, the case is given a low fitness value.

2. Mesh Approach

For all airfoils, the near-body grid is generated using Chimera Grid Tools (CGT) 2.3.[81] Two body-fitted grids model each airfoil and are embedded in a Cartesian background mesh (not shown) that extends 50 chord lengths from the airfoil in all directions. Flow variables are interpolated between grids at the overset boundaries in a manner that preserves the full accuracy of the solver.

The body fitted grids have a split-O topology, as shown in Fig. 12, which is necessary to accommodate the grid adaption scheme available in OVERFLOW 2.2o.[82] Grid adaption is not pursued in the present work due to the added computational cost, but it is preserved as an option for further analysis of specific geometries and flow regimes.
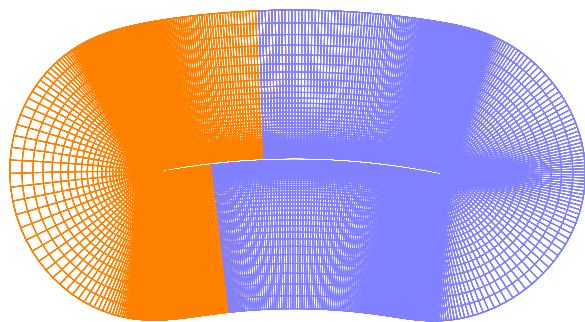
Fig. 12   Near body grid for a cambered plate airfoil.

The grids place approximately 800 points around the airfoil with the points clustered to ensure geometric fidelity and accurate capture of the flow gradients. Grid stretching ratios in all directions do not exceed 10%. The spacing normal to the airfoil surface places the first point at $y^+ < 1$. Airfoil surfaces are modeled with a viscous boundary condition, and the far field boundaries are modeled using a freestream characteristic boundary condition.

3. Two-Dimensional Versus Three-Dimensional Analysis

It is important to note that ultimately the cost of repeated fitness function evaluation by the optimization (i.e. the RANS CFD cases) is the prohibitive segment in using this GA for many separate optimizations. Therefore, all analyses presented will be analyzed using a two-dimensional approach in an effort to reduce computational cost. Two-dimensional airfoil analysis can yield accurate results as long as the assumption of predominantly two-dimensional flow is valid.

Hoarau et al.[34] examine the NACA 0012 airfoil using DNS for $800 < Re_c < 10,000$ and conclude that for coherent large-scale structures in the near-field a two-dimensional approximation is valid. The difference between the two- and three-dimensional computations did not exceed about 10% in the study.

At a high enough angle of attack, three-dimensional flow is expected as spanwise instabilities appear and the vortices become incoherent and ultimately break down into turbulent flow. Both Balzer and Fasel[23] and Munday et al.[45] conclude for low Reynolds numbers and different airfoils that breakdown to three-dimensional flow occurs at an angle of attack of around $6° < \alpha < 8°$.

B. Validation of Numerical Approach

To validate the approach in the preceding section, a set of validation cases is presented.

1. Triangular airfoil at $Re_c = 3,000$

Munday et al.[45] analyze a triangular airfoil using a Mars wind tunnel and (three-dimensional) Direct Numerical Simulations (DNS) at a Reynolds number of $Re_c = 3,000$ for $M = 0.15$ and $M = 0.50$. The airfoil has a maximum thickness of $t/c = 0.05$ and the apex is located at $x/c = 0.30$, see Fig. 13.
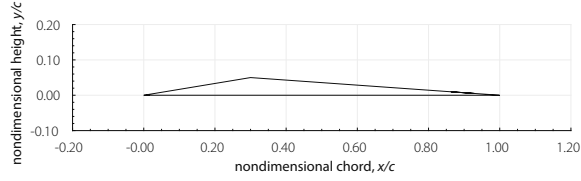
Fig. 13 Triangular airfoil as analyzed by Munday et al.[45]

Fig. 14 shows the comparison between the mean section lift and drag coefficients from the present study and Munday et al. at $Re_c = 3,000$ for $M = 0.15$. The shaded areas around the averaged OVERFLOW results indicate the approximate standard deviation of the unsteady results.
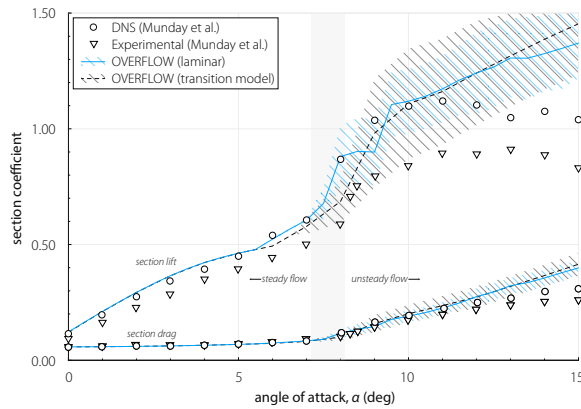

Fig. 14 Comparison of section coefficients at Re_c = 3,000 for M = 0.15, DNS and experimental results from Munday et al.[45]

OVERFLOW results are shown for simulations run fully laminar or with a transition model. As the freestream turbulence intensity was reported to be less then $Tu_\infty < 1\%$ the transition model simulations were run with the OVERFLOW standard freestream turbulence intensity of around $Tu_\infty \cong 0.082\%$. It can be seen that the lift prediction from the laminar calculation is slightly better at $\alpha = 7°$, until both methods diverge from both DNS and experimental results at higher angles of attack as unsteady flow commences. The correlation between OVERFLOW results and DNS results is slightly improved at $M = 0.50$, as shown in Fig. 15.

For $M = 0.50$, the onset of stall is delayed to higher angles of attack and both OVERFLOW simulations perform similarly. Munday et al. indicate that the transition from steady to unsteady flow is delayed with increasing Mach

number, which is captured by OVERFLOW based on the increase of the standard deviation from the mean around the predicted angles from three-dimensional flow. The divergence of the RANS cases versus DNS (or experimental) results is expected after that as the OVERFLOW cases are truly two-dimensional (not allowing three-dimensional structures to develop), and RANS-based methods are inherently limited at predicting stall or substantially separated flow. The discrepancy between experimental and DNS results is not known at this point.
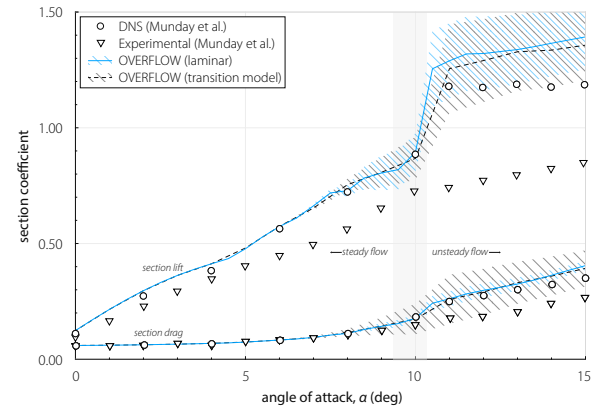
Fig. 15 Comparison of section coefficients at Re_c = 3,000 for M = 0.50, DNS and experimental results from Munday et al.[45]

The time-averaged pressure profiles over the airfoil are presented in Fig. 16 and Fig. 17 for $M = 0.15$ and $M = 0.50$, respectively.
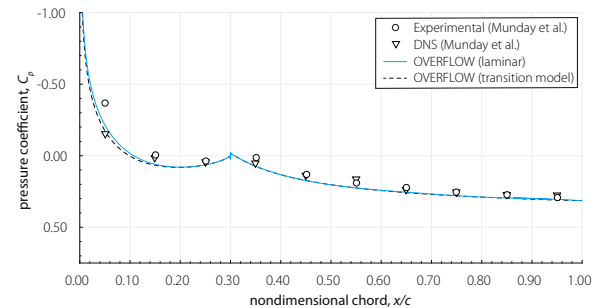

Fig. 16 Pressure coefficient on the upper surface at α = 6°, M = 0.15, DNS and experimental results from Munday et al.[45]

The reference pressure is taken to be the pressure at the apex of the airfoil at $x/c = 0.30$, as presented by Munday et al. Simulations run fully laminar and with transition model both show good agreement for the upper surface pressure distribution at both Mach numbers.
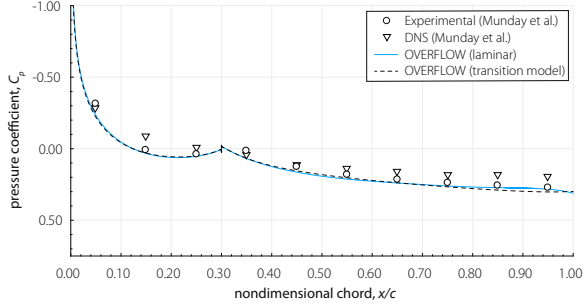
Fig. 17 Pressure coefficient on the upper surface at $a = 6°$, $M = 0.50$, DNS and experimental results from Munday et al.[45]

2. Plate with leading and trailing edge flaps at $Re_c = 40,000$

Koning et al.[10] and Traub and Coffman[39] independently found that a double-edged plate (or flat plate with leading and trailing edge flaps) can provide significant improvements in aerodynamic performance over a 5% circular arc profile. The most effective flapped geometry as found by Traub and Coffman is recreated and is shown in Fig. 18. It shows a plate with thickness $t/c = 0.008$ and downward leading and trailing edge flap deflection of 15 degrees at $x/c = 0.10$ and $x/c = 0.80$, respectively.
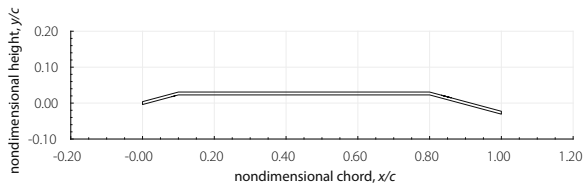
Fig. 18 Plate with leading and trailing edge flaps, from Traub and Coffman[39]

The low-speed windtunnel used for the experimental testing has a measured turbulence intensity of $Tu_\infty = 0.24\%$, which is used in the transition model based simulations to reflect the appropriate amplification factor. Only tests performed at $Re_c = 40,000$ are investigated here, as the other Reynolds numbers fall outside of the Reynolds number scope in the present work. The section lift-drag polar for the flapped plate is shown in Fig. 19.

The section lift-to-drag ratio versus section lift coefficient is shown in Fig. 20. It can be seen that in the region of peak lift-to-drag ratio, the laminar simulations correlate better than the transition model simulations. The differences are stronger

than for the triangular airfoil correlations (see Fig. 14) due to the higher Reynolds number.
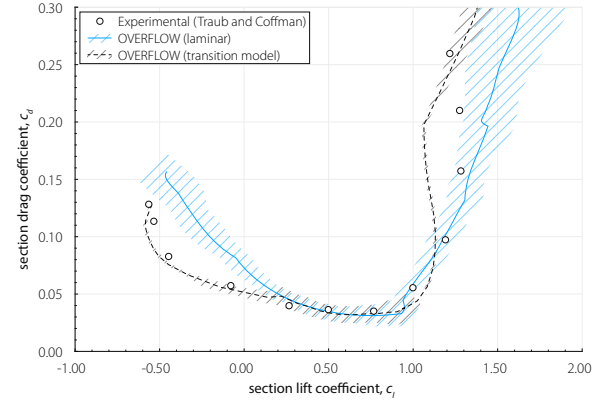
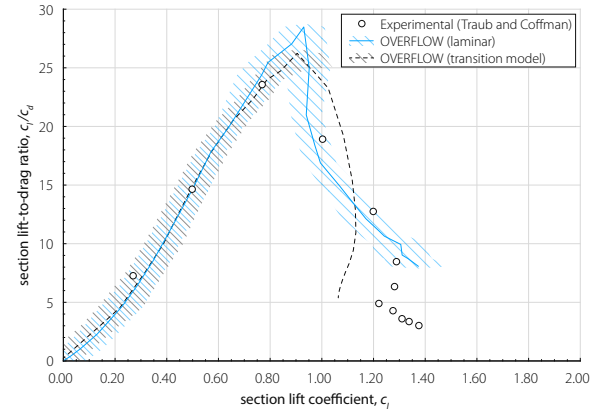**Fig. 19 Lift-drag polar at $Re_c = 40,000$, experimental results from Traub and Coffman[39]**

Fig. 20 Lift-to-drag ratio at $Re_c = 40,000$, experimental results from Traub and Coffman[39]

The primary region of interest in the present work is the region where the lift-to-drag is maximized. Despite the lack of sufficient data points to indicate the peak lift-to-drag ratio, the laminar calculations show the best correlation.

3. Transition Modeling and Laminar Calculations

The previous two validation cases showed the close matches of the laminar cases versus the transition model based cases. The optimized double-edged plate airfoil from Koning et al,[10] shown in Fig. 21, is used here to investigate the differences at these conditions of running laminar versus running with a transition model. The SA-AFT2017b model determines the critical amplification factor, N_{crit}, as a function of the free-stream turbulence intensity, Tu_∞, based upon Drela's modification of Mack's relation.[79,83]

$$\tau = 2.5\tanh(Tu_\infty/2.5)$$

$$N_{crit} = -8.43 - 2.4\ln\left(\frac{\tau}{100}\right)$$

The transition model simulations were run with the OVERFLOW standard freestream turbulence intensity of around $Tu_\infty \cong 0.082\%$, resulting in an amplification factor of around $N_{crit} \cong 8.6$. It is unclear if modification of this factor could improve rotor performance predictions by either reducing the amplification factor to account for various external disturbances/receptivity, or increasing the amplification factor to account for favorable centrifugal forces acting on the boundary layer.[14]
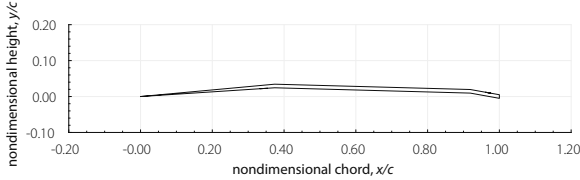
Fig. 21 Optimized double-edged plate for Re = 16,862 and M = 0.52, from Koning et al.[10]

The lift curve is plotted for $Re/M = 33,724$ and $M = 0.30, 0.50, 0.70$ in Fig. 22, Fig. 23, and Fig. 24, respectively. The Re/M ratio is representative for operating conditions of Mars rotors.[2] The ratio is fixed as Reynolds number will scale with RPM and thus with Mach number for rotor operation.
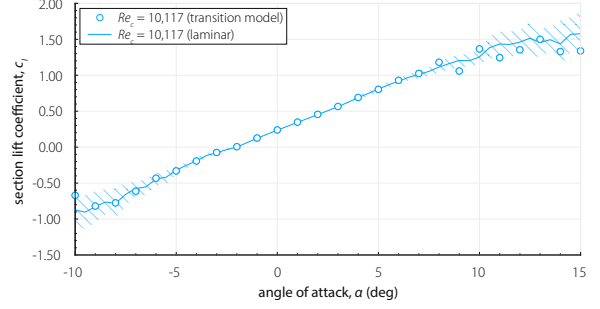
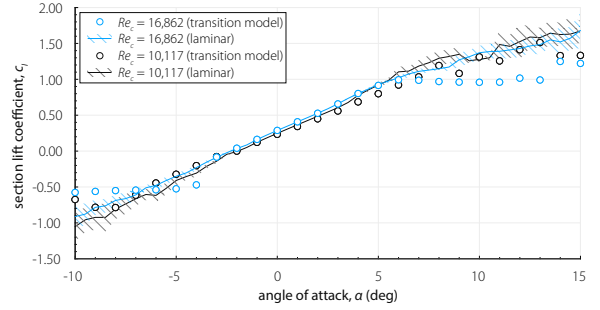**Fig. 22 OVERFLOW lift curve for Re/M = 33,724 (Re = 10,117) for M = 0.30.**

Fig. 23 OVERFLOW lift curve for Re/M = 33,724 (Re = 16,862) and Re = 10,117 for M = 0.50.
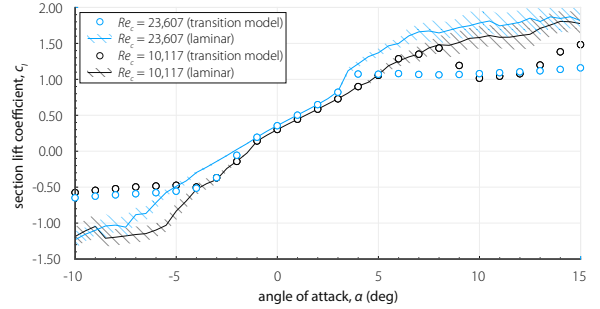
Fig. 24 OVERFLOW lift curve for Re/M = 33,724 (Re = 23,607) and Re = 10,117 for M = 0.70.

The laminar and transition model based simulations agree well in the linear regime and progressively start to diverge for increased Reynolds numbers at angles of attack off-peak efficiencies. For constant Reynolds number, however, the Mach number variation has a much less pronounced effect on transition model influence. The lift-to-drag ratio versus section lift coefficient for $Re/M = 33,724$ and $M = 0.30, 0.50$, and $M = 0.70$ is shown in Fig. 25, Fig. 26, and Fig. 27, respectively.
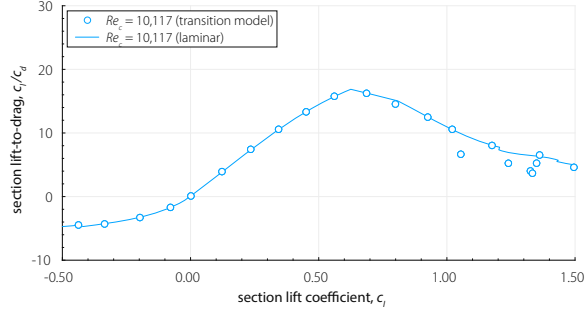
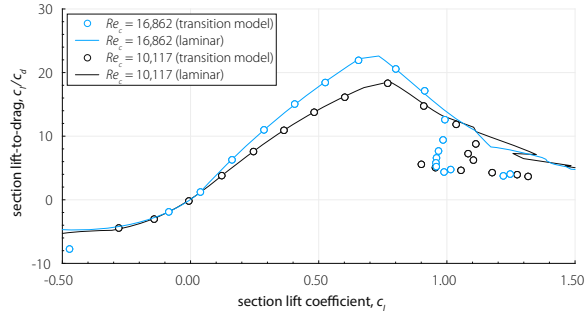**Fig. 25 OVERFLOW Lift-to-drag ratio for Re/M = 33,724 (Re = 10,117) for M = 0.30.**

Fig. 26 OVERFLOW Lift-to-drag ratio for Re/M = 33,724 (Re = 16,862) and Re = 10,117 for M = 0.50.
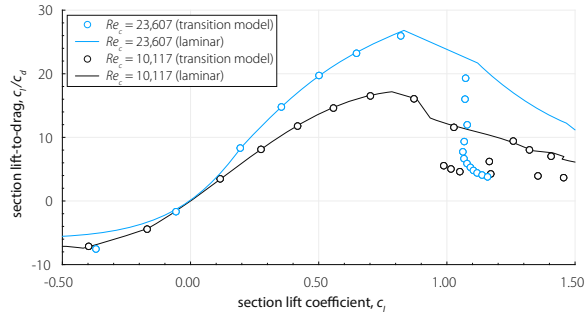

Fig. 27 OVERFLOW Lift-to-drag ratio for Re/M = 33,724 (Re = 23,607) and Re = 10,117 for M = 0.70.

With increasing Reynolds number, the transition model predicts more rapid deterioration of the drag coefficient at stable section lift coefficients. The laminar and transition model based simulations agree well in the pre-stall, positive lift-to-drag ratio region. Similarly, for constant Reynolds number, however, the Mach number variation has a much less pronounced effect on laminar-turbulent transition.

The amplification factor and modified intermittency for an angle of attack of $\alpha = 5°$ at $Re_c = 10{,}117$ for $M = 0.30$ is shown in Fig. 28 and Fig. 29, respectively. The amplification factor

is highest in the separated shear layer and in the vortex cores, with the largest values only attained downstream of the trailing edge. The modified intermittency shows near-laminar flow around the airfoil, despite the amplification factor increase in the shear layer and upper surface unsteady flow.
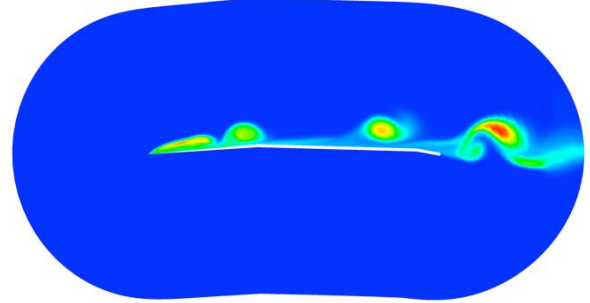

Fig. 28 Amplification factor at α = 5.0°, Re = 10,117 for M = 0.30; highest amplification factor in red, $\tilde{n}_{max}$ = 7.2 (transition model, time-accurate).
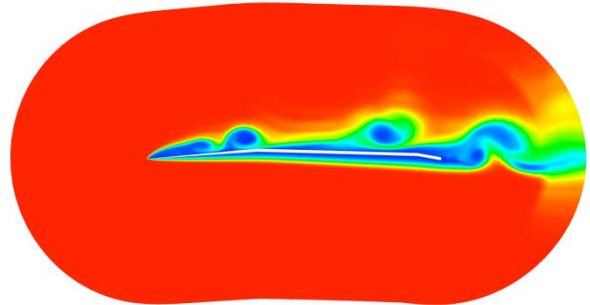

Fig. 29 Modified intermittency at α = 5.0°, Re = 10,117 for M = 0.30; blue regions indicate laminar flow (transition model, time-accurate).

At a Mach number of around $M = 0.50$, it is expected that laminar calculations up to a section lift coefficient of $c_l \cong 1.00$ will provide the same performance as one with a transition model. For higher Mach numbers and angles-of-attack out of the linear regime, it is clear that a transition model is needed to approximate transitional turbulent flow.

VI. Optimization Results

Airfoil optimization is performed for the outboard stations (stations 3, 4, and 5) of a concept rotor design for an advanced Mars Science Helicopter (MSH). The planform is shown in Fig. 30.
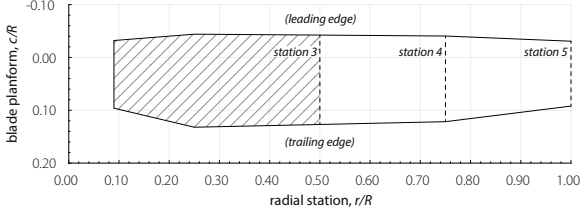

Fig. 30   Rotor planform for advanced Mars Helicopter.

It is at this stage assumed that the outboard regions can be manufactured using a 1% thick plate-type airfoil. The Re/M values in the Mars atmosphere for 2400 RPM are displayed in Table 5. Additionally, a station 5 optimization at $M = 0.90$ is performed (for equal Re/M) to investigate tip airfoil shapes for higher forward flight speeds. All optimizations are performed both using a cambered plate (CP) optimization and a double-edged plate (DEP) optimization.

Table 5   Reynolds-Mach combinations for hover operation.

Case	Airfoil	Station	Re_c/M	M	Re_c
1	CP	3	33,511	0.35	11,729
2	DEP				
3	CP	4	32,427	0.52	16,862
4	DEP				
5	CP	5	24,321	0.70	17,024
6	DEP				
7	CP		24,321	0.90	21,889
8	DEP				

A. Objective Space: Pareto Front

The optimization results are converted from their fitness values f_1 and f_2 to the mean sectional lift and drag coefficients c_{l_μ} and c_{d_μ}, respectively. The subscript μ is left out for clarity, but all sectional coefficients represent the mean value over the converged integrated forces. While the computed Pareto fronts demonstrate that there are airfoils capable of superior performance to the clf5605 airfoils at each lift coefficient, it is not evident from this figure that any single, optimum airfoil is superior to the clf5605 airfoil at *every lift coefficient.*

1. Cambered Plate (CP) Optimization

The Pareto front for cambered plate (CP) cases is shown in Fig. 31 for case 1, 3, and 5. Below, on the same sectional lift coefficient scale, the section lift-to-drag ratio is presented. Each datapoint represents a single airfoil, and the Pareto front (or Pareto optimal set) consists therefore of multiple airfoils. The single objective optimization (SOO) results from Koning et al.[10] to show the full convergence for $c_l \approx 0.70$.
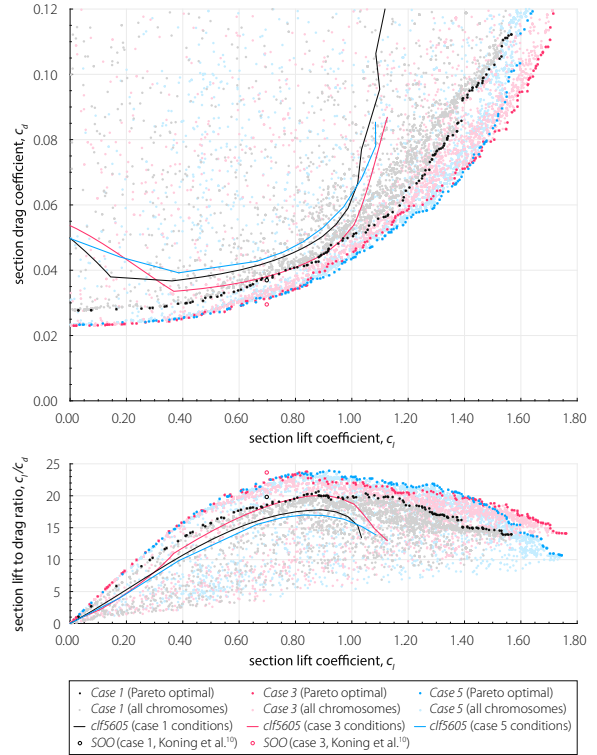

Fig. 31   Optimization results for cambered plate (CP) airfoils: Section drag and section lift-to-drag ratio versus section lift coefficient for case 1, 3, and 5.

For each of the conditions, the aerodynamic performance of the outboard airfoil of the Mars Helicopter, the clf5605 airfoil as shown in Fig. 32, is shown for comparison.
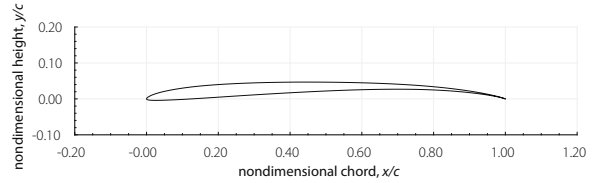

Fig. 32   Outboard airfoil on Mars Helicopter ($r/R > 0.50$), from Koning et al.[2]

2. Double-Edged Plate (DEP) Optimization

The Pareto front for double-edged plate (DEP) cases is shown in Fig. 34 for case 2, 4, and 6. For both CP and DEP optimization, the section lift-to-drag ratio of the optimized airfoils on the Pareto front is always higher than the MH outboard airfoil at equal section lift.
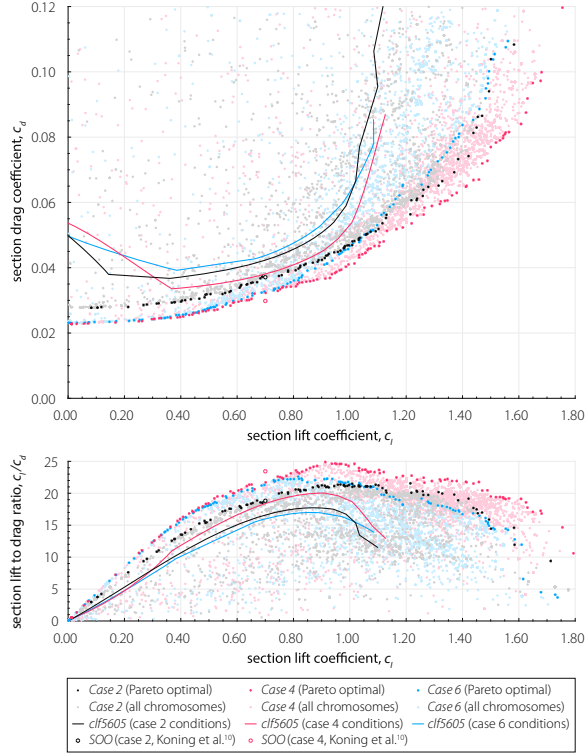

Fig. 33 Optimization results for double-edged plate (DEP) airfoils: Section drag and section lift-to-drag ratio versus section lift coefficient for case 2, 4, and 6.

The Pareto front shows drag minimization and lift maximization efforts with a peak section lift-to-drag ratio of $(c_l/c_d)_{max} \approx 25.20$ at $c_l \approx 0.93$ for $M = 0.52$.

B. Decision Space: Parameter Variation

From the Pareto optimal set, information can be deduced as to what geometry variation results in the highest efficiency for a design lift coefficient.

1. Cambered Plate (CP) Geometry

For the cambered plate (CP) genes, the individual decision variables can be generalized to obtain the maximum camber, the location of the maximum camber, the leading edge slope, and the

angle of attack. Their dependency can be observed over the lift coefficient range of the Pareto front. The airfoil parameters are summarized in Fig. 34 for case 1, 3, and 5. Table 1 shows the base constraints for the cambered plate geometry, and Table 2 elaborates on the geometric meaning of the decision variables. From genes 1-4, the Bézier curve is computed, which allows computation of the location and magnitude of the maximum camber. Gene 5 corresponds to the angle of attack.
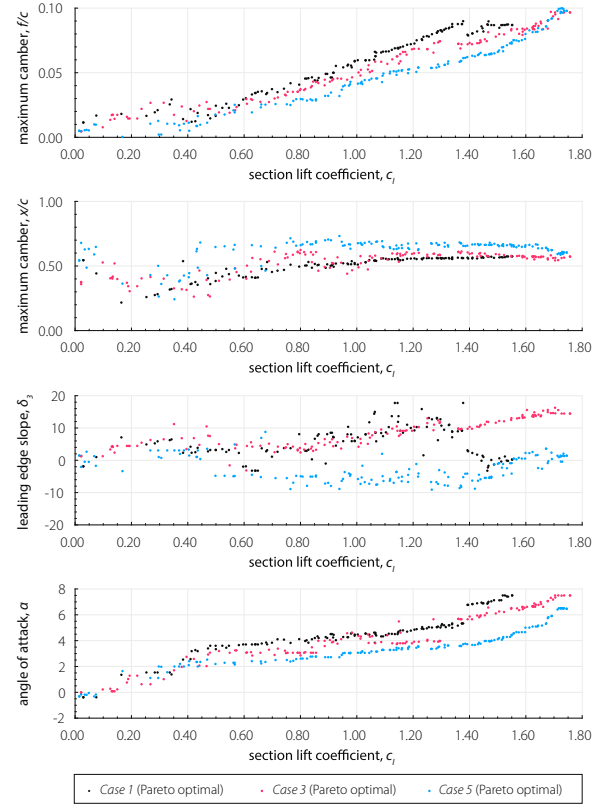

Fig. 34 Optimization results for cambered plate (CP) airfoils: decision variables/genes versus section lift coefficient for case 1, 3, and 5.

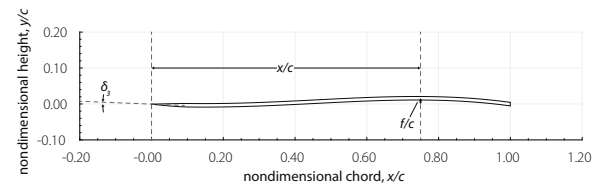The parameters discussed in Fig. 34 are schematically presented in Fig. 35.

Fig. 35 Definition of parameters for CP airfoil.

The magnitude and location of the maximum camber are observed to increase steadily with lift coefficient over the Pareto front for all Mach numbers. Near and beyond peak efficiency the location of maximum camber is nearly constant between $0.50 < x/c < 0.70$. The results show that for a cambered plate airfoil the optimal location of maximum camber is between $0.50 < x/c < 0.60$ and the camber magnitude is proportional to the design lift coefficient. There is only slight influence of the Mach number on optimal airfoil shape, with the exception of the leading edge slope variation.

2. Double-Edged Plate (DEP) Geometry

For the double-edged plate genes, the individual decision variables can be generalized to obtain the chordwise locations of the edges, the angles of the leading- and trailing-edge deflections, and the angle of attack. The airfoil parameters are schematically presented in Fig. 36.

Table 3 shows the base constraints for the double-edged plate geometry, and Table 4 elaborates on the geometric meaning of the decision variables. The airfoil parameters are summarized in Fig. 37 for case 2, 4, and 6.
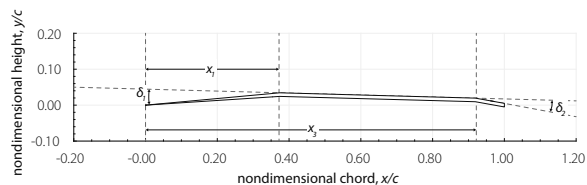

Fig. 36   Definition of parameters for DEP airfoil.

From genes 1-4 the leading -and trailing-edge angles are computed (with respect to the upper surface). Genes 1 and 3 correspond to the x-coordinate of the leading- and trailing-edge edges respectively. Gene 5 corresponds to the angle of attack.

The results for the hinge locations (gene 1 and 3) and the leading edge angle show scatter at low lift coefficients ($c_l \lesssim 0.70$), which is primarily due to the fact that the x-coordinate is not influential when a flat plate is approximated near zero-lift. At high post peak section lift-to-drag ratios ($c_l > 1.00$) the scatter also increases due to the onset of stall. Near peak performance ($0.70 < c_l < 1.00$) the Pareto optimal results show the least scatter.

For the design of a double-edged plate the Mach number has considerable influence on the location and angle of the leading edge deflection. The trailing edge location for the Pareto optimal set for moderate lift coefficients is rather constant at $x/c = 0.80$. The leading edge angle, trailing edge angle, and angle of attack are proportional to the design lift coefficient.
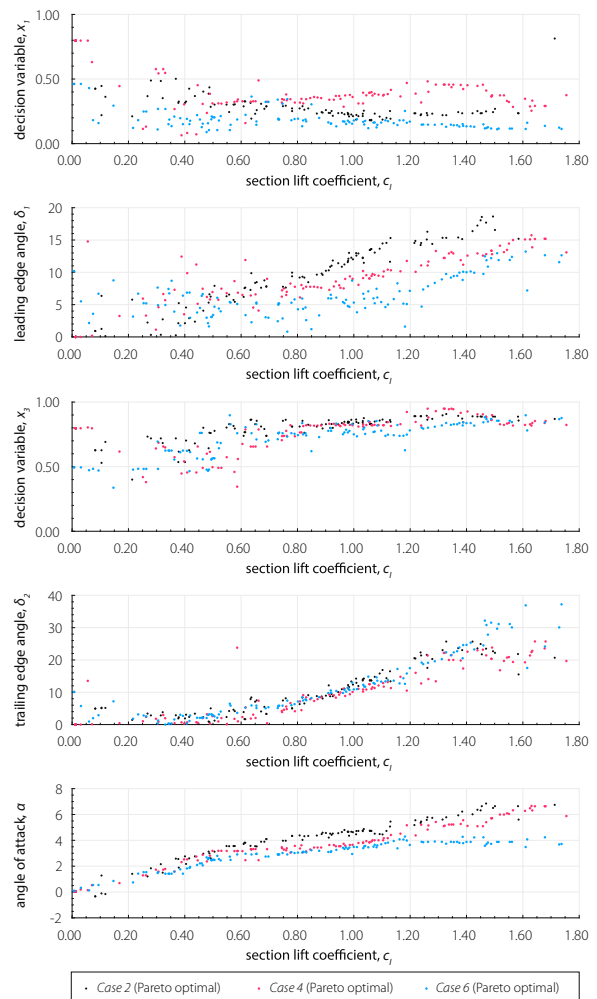

Fig. 37   Optimization results for double-edged plate (DEP) airfoils: decision variables/genes versus section lift coefficient for case 2, 4, and 6.

C.   Airfoil Shapes

The airfoil with the highest attained lift-to-drag ratio for case 3 and case 4 is shown in Fig. 38 and Fig. 39, respectively. The velocity magnitudes are shown at the angle of attack for highest efficiency. Both cases at M = 0.52 show shed vortices at the peak performance, indicating

the vortices are in this case beneficial to the performance of the airfoil through their low pressure cores.

An example of the variation of airfoil profile over a Pareto optimal set is shown for case 3 and 6 in Fig. 40.
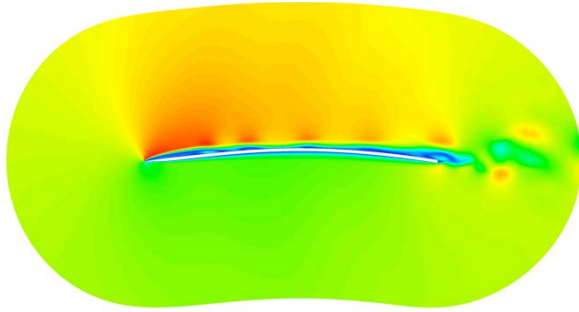

Fig. 38 Velocity magnitude for highest attained lift-to-drag ratio in case 3, $\alpha = 3.5°$ (transition model, time-accurate).
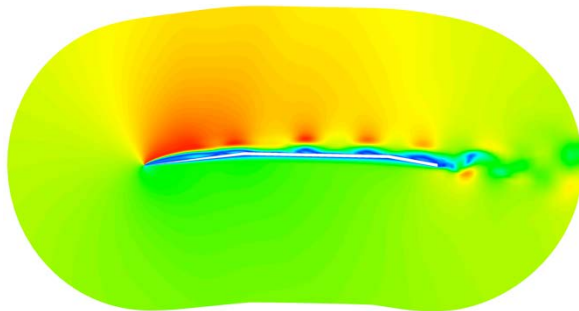

Fig. 39 Velocity magnitude for highest attained lift-to-drag ratio in case 4, $\alpha = 4.0°$ (transition model, time-accurate).
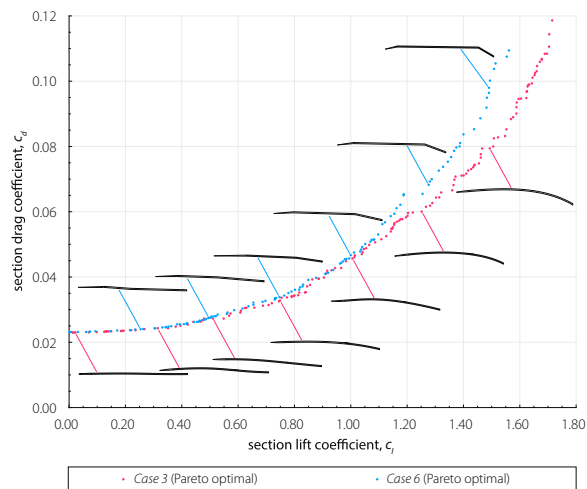

Fig. 40 Airfoil geometry variation over the Pareto optimal set for case 3 and 6.

D. High Subsonic Mach Performance

The thin optimized profiles naturally have an advantage over the clf5605 airfoil due to its 5% airfoil thickness. The CP and DEP optimized airfoils for $M = 0.90$ are shown in Fig. 41.
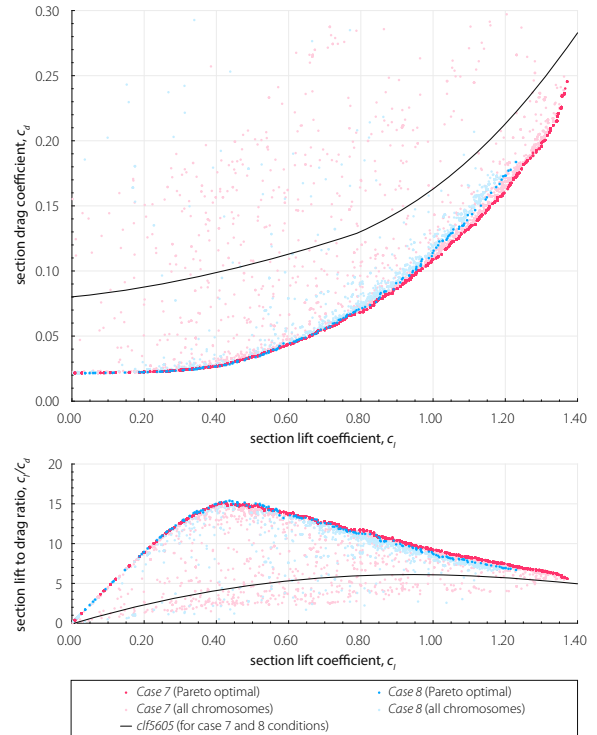
Fig. 41 Optimization results for $M = 0.90$: Section drag and section lift-to-drag ratio versus section lift coefficient for case 7 and 8.

The results show that during forward flight maneuvers, the benefit of a thin (optimized) tip airfoil results in substantial airfoil efficiency improvements.

E. Performance Overview

The peak lift-to-drag ratios for each case are summarized in Table 6. The peak lift-to-drag ratio for the outboard airfoil of the Mars Helicopter, clf5605, is presented for the same operating conditions. The difference column indicates the percent difference from cases 1-8 compared to the clf5605 peak lift-to-drag ratio for each respective condition.

For all Pareto optimal sets the peak lift-to-drag ratio is achieved at $0.80 < c_l < 1.00$, except for cases at $M = 0.90$ where it occurs around $c_l = 0.45$.

Table 6 Reynolds-Mach combinations for hover operation.

Case	Airfoil	Re_c	M	$(c_l/c_d)_{max}$	clf5605	difference
1	CP	11,729	0.35	20.68	17.79	16.8%
2	DEP			21.56		21.1%
3	CP	16,862	0.52	23.78	20.03	18.7%
4	DEP			25.20		25.8%
5	CP	17,024	0.70	23.92	16.98	40.9%
6	DEP			22.61		33.2%
7	CP	21,889	0.90	14.93	6.25	238.88%[§]
8	DEP			15.38		246.08%

VII. Conclusion

Unconventional airfoil shapes with sharp leading edges are explored and optimized for aerodynamic performance at representative Reynolds-Mach combinations for a concept Mars rotor. Sharp leading edges initiate immediate flow separation at the leading edge, and the occurrence of large-scale vortex shedding is found to contribute to the relative performance increase of the optimized airfoils, compared to conventional airfoil shapes.

The oscillations are shown to occur independent from laminar-turbulent transition, and transition modeling is shown to be necessary at the higher end of the Reynolds number range considered and/or at very high angles of attack. The influence of the Mach number on laminar-turbulent transition is found to be low in the current regime.

Pareto optimal sets are shown for various operating conditions and general design considerations for a cambered plate or double-edged plate in this regime are deduced. Comparisons are presented to the performance of the outboard Mars Helicopter airfoil. Peak lift-to-drag ratio increases between 17% and 41% are observed for similar section lift, indicating the beneficial performance of plate-type airfoils for low Reynolds number applications.

VIII. Future Work

The wings of various insects and birds operate at similar Reynolds numbers to the Mars Helicopter rotor. Dragonflies, locusts, and swifts are all able to glide,[62,84,85] making their airfoil profiles of interest for steady or rotary wing optimization for the design of airfoils at the Reynolds number range under consideration. These airfoils usually contain large-scale chordwise corrugations that are associated with the dynamics of the laminar separation bubble formation for swifts and dragonflies,[59,61,62] and are observed to reduce integrated force fluctuations leading to lower mean drag (as compared to the Eppler E-61 airfoil).[58]

Optimization for the inboard sections (stations 1 and 2) of the rotor design will require thicker profiles for structural considerations. This opens up various possible design and optimization approaches such as a polygonal airfoils[10] at fixed thickness, or airfoil corrugations as they are found to improve the structural stiffness of the wing for dragonfly airfoils.[59,86]

For more detailed design, Pareto front quality enhancements (through both evaluation of higher number of generations and algorithm improvements) are required. This will also allow a fair comparison between the different airfoil types.

Further studies will also look into pressure and skin friction distributions over the airfoil to investigate the flow physics and the performance contributions of the top and bottom surfaces of the airfoil.

Acknowledgments

[§] At different section lift coefficients, see Fig. 41.

References

[1]   Balaram, J. (Bob), Canham, T., Duncan, C., Golombek, M., Grip, H. F., Johnson, W., Maki, J., Quon, A., Stern, R., and Zhu, D., "Mars Helicopter Technology Demonstrator," *AIAA Science and Technology Forum and Exposition (AIAA SciTech)*, 2018.
      doi:10.2514/6.2018-0023

[2]   Koning, W. J. F., Johnson, W., and Allan, B. G., "Generation of Mars Helicopter Rotor Model for Comprehensive Analyses," *AHS Aeromechanics Design for Transformative Vertical Flight*, San Francisco, California: 2018.

[3]   Koning, W. J. F., Johnson, W., and Grip, H. F., "Improved Mars helicopter aerodynamic rotor model for comprehensive analyses," *AIAA Journal*, vol. 57, 2019, pp. 3969–3979.
      doi:10.2514/1.J058045

[4]   Balaram, J. (Bob), Daubar, I. J., Bapst, J., and Tzanetos, T., "Helicopter on Mars: Compelling Science of Extreme Terrains Enabled by an Aerial Platform," *9th International Conference on Mars*, Pasadena, California: 2019.

[5]   Tzanetos, T., "Mars Science Helicopter" Available: https://www-robotics.jpl.nasa.gov/tasks/showTask.cfm?FuseAction=ShowTask&TaskID=353&tdaID=700145.

[6]   Carmichael, B. H., "Low Reynolds Number Airfoil Survey, Volume 1," NASA CR-165803-VOL-1, 1981.

[7]   Lissaman, P. B. S., *"Low-Reynolds-Number Airfoils,"* Annual Review of Fluid Mechanics, Vol. 15, Jan. 1983, pp. 223–239.
      doi:10.1146/annurev.fl.15.010183.001255

[8]   Mueller, T. J., and DeLaurier, J. D., *"Aerodynamics of Small Vehicles,"* Annual Review of Fluid Mechanics, Vol. 35, Jan. 2003, pp. 89–111.
      doi:10.1146/annurev.fluid.35.101101.161102

[9]   Koning, W. J. F., Romander, E. A., and Johnson, W., "Low Reynolds Number Airfoil Evaluation for the Mars Helicopter Rotor," *AHS International 74th Annual Forum & Technology Display*, Phoenix, Arizona: 2018.

[10] Koning, W. J. F., Romander, E. A., and Johnson, W., "Performance Optimization of Plate Airfoils for Martian Rotor Applications Using a Genetic Algorithm," *45th European Rotorcraft Forum*, Warsaw, Poland: 2019, pp. 1–15.

[11] Schlichting, H., and Kestin, J., *Boundary-Layer Theory*, 7th ed., McGraw–Hill, New York, 1979, Chaps. 2, 7, 10, 13, 16, 17.

[12] Drela, M., *Flight vehicle aerodynamics*, MIT press, 2014.

[13] Hoerner, S. F., *Fluid-Dynamic Drag: Practical Information on Aerodynamic Drag and Hydrodynamic Resistance*, Hoerner Fluid Dynamics, Bricktown, NJ, 1965, Chaps. 3, 5, 6, 15, 19.

[14] Schmitz, F. W., "Aerodynamics of the Model Airplane. Part 1—Airfoil Measurements," NASA TM-X-60976, 1967

[15] O'Meara, M., and Mueller, T. J., "Laminar separation bubble characteristics on an airfoil at low Reynolds numbers," *AIAA Journal*, vol. 25, Aug. 1987, pp. 1033–1041.
      doi:10.2514/3.9739

[16] Fitzgerald, E. J., and Mueller, T. J., "Measurements in a separation bubble on an airfoil using laser velocimetry," *AIAA journal*, vol. 28, 1990, pp. 584–592.
      doi:10.2514/3.10433

[17] McMasters, J., and Henderson, M., "Low-Speed Single-Element Airfoil Synthesis," Technical Soaring, Vol. 6, No. 2, 1980, pp. 1–21.

[18] Roberts, W. B., "Calculation of laminar separation bubbles and their effect on airfoil performance," *AIAA journal*, vol. 18, 1980, pp. 25–31.
      doi:10.2514/3.50726

[19] Boutilier, M. S. H., and Yarusevych, S., "Separated shear layer transition over an airfoil at a low Reynolds number," *Physics of Fluids*, vol. 24, 2012, p. 84105.
      doi:10.1063/1.4744989

[20] Saric, W. S., Reed, H. L., and Kerschen, E. J., "Boundary-layer receptivity to freestream disturbances," *Annual review of fluid mechanics*, vol. 34, 2002, pp. 291–319.
      doi:10.1146/annurev.fluid.34.082701.161921

[21] Boiko, A. V, Dovgal, A. V, Grek, G. R., and Kozlov, V. V, *Physics of Transitional Shear Flows: Instability and Laminar–Turbulent Transition in Incompressible Near-Wall Shear Layers*, Springer Science & Business Media, 2011.

[22] Fisher, A., "The effect of freestream turbulence on fixed and flapping micro air vehicle wings," 2013.

[23] Balzer, W., and Fasel, H., "Direct numerical simulation of laminar boundary-layer separation and separation control on the suction side of an airfoil at low Reynolds number conditions," *40th Fluid Dynamics Conference and Exhibit*, 2010, p. 4866.
      doi:10.2514/6.2010-4866

[24] KERSCHEN, E., "Boundary layer receptivity," *12th Aeroacoustic Conference*, 1989, p. 1109.

[25] Simoni, D., Lengani, D., Ubaldi, M., Zunino, P., and Dellacasagrande, M., "Inspection of the dynamic properties of laminar separation bubbles: free-stream turbulence intensity effects for different Reynolds numbers," *Experiments in Fluids*, vol. 58, 2017, p. 66.
      doi:10.1007/s0034

[26] Laitone, E. V., "Wind Tunnel Tests of Wings at Reynolds Numbers Below 70000," *Experiments in Fluids*, Vol. 23, Nov. 1997, pp. 405–409.
      doi:10.1007/s003480050128

[27] Wang, S., Zhou, Y., Alam, M. M., and Yang, H., "Turbulent Intensity and Reynolds Number Effects on an Airfoil at Low Reynolds Numbers," *Physics of Fluids*, Vol. 26, Nov. 2014, Paper 115107.
      doi:10.1063/1.4901969

[28] van Ingen, J. L., "The eN Method for Transition Prediction. Historical Review of Work at TU Delft," 38th Fluid Dynamics Conference and Exhibit, AIAA Paper 2008-3830, 2008.
doi:10.2514/6.2008-3830

[29] Pauley, L. L., Moin, P., and Reynolds, W. C., "The Structure of TwoDimensional Separation," Journal of Fluid Mechanics, Vol. 220, Nov. 1990, pp. 397–411.
doi:10.1017/S0022112090003317

[30] Abdalla, I. E., and Yang, Z., "Numerical study of the instability mechanism in transitional separating–reattaching flow," *International Journal of Heat and Fluid Flow*, vol. 25, 2004, pp. 593–605.
doi:10.1016/j.ijheatfluidflow.2004.01.004

[31] Yarusevych, S., Sullivan, P. E., and Kawall, J. G., "Coherent structures in an airfoil boundary layer and wake at low Reynolds numbers," *Physics of Fluids*, vol. 18, 2006, p. 44101.
doi:10.1063/1.2187069

[32] Windte, J., Scholz, U., and Radespiel, R., "Validation of the RANS-simulation of laminar separation bubbles on airfoils," *Aerospace science and technology*, vol. 10, 2006, pp. 484–494.
doi:10.1016/j.ast.2006.03.008

[33] Alam, M. M., Zhou, Y., Yang, H. X., Guo, H., and Mi, J., "The ultra-low Reynolds number airfoil wake," *Experiments in fluids*, vol. 48, 2010, pp. 81–103.
doi:10.1007/s00348-009-0713-7

[34] HOARAU, Y., BRAZA, M., Ventikos, Y., Faghani, D., and Tzabiras, G., "Organized modes and the three-dimensional transition to turbulence in the incompressible flow around a NACA0012 wing," *Journal of Fluid Mechanics*, vol. 496, 2003, pp. 63–72.
doi:10.1017/S0022112003006530

[35] Gaster, M., "The Structure and Behaviour of Laminar Separation Bubbles," HM Stationery Office R&M 3595, London, 1969.

[36] Huang, R. F., and Lin, C. L., "Vortex Shedding and Shear-Layer Instability of Wing at Low-Reynolds Numbers," *AIAA Journal*, Vol. 33, No. 8, 1995, pp. 1398–1403.
doi:10.2514/3.12561

[37] Yarusevych, S., Sullivan, P. E., and Kawall, J. G., "On Vortex Shedding from an Airfoil in Low-Reynolds-Number Flows," *Journal of Fluid Mechanics*, Vol. 632, Aug. 2009, pp. 245–271.
doi:10.1017/S0022112009007058

[38] Hoffmann, J. A., "Effects of freestream turbulence on the performance characteristics of an airfoil," *AIAA journal*, vol. 29, 1991, pp. 1353–1354.
doi:10.2514/3.10745

[39] Traub, L. W., and Coffman, C., "Efficient Low-Reynolds-Number Airfoils," *Journal of Aircraft*, vol. 56, 2019, pp. 1987–2003.
doi:10.2514/1.C035515

[40] Sunada, S., Sakaguchi, A., and Kawachi, K., "Airfoil Section Characteristics at a Low Reynolds Number," *Journal of Fluids Engineering*, Vol. 119, March 1997, pp. 129–135.
doi:10.1115/1.2819098

[41] Laitone, E. V, "Aerodynamic lift at Reynolds numbers below 7 x 10 exp 4," *AIAA journal*, vol. 34, 1996, pp. 1941–1942.
doi:10.2514/3.13329

[42] Winslow, J., Otsuka, H., Govindarajan, B., and Chopra, I., "Basic Understanding of Airfoil Characteristics at Low Reynolds Numbers (104–105)," *Journal of Aircraft*, Dec. 2017, pp. 1–12.
doi:10.2514/1.C034415

[43] Boiko, A. V, Grek, G. R., Dovgal, A. V, and Kozlov, V. V, *The origin of turbulence in near-wall flows*, Springer Science & Business Media, 2013.
doi:10.1007/978-3-662-04765-1

[44] Arena, A. V., and Mueller, T. J., "Laminar Separation, Transition, and Turbulent Reattachment near the Leading Edge of Airfoils," *AIAA Journal*, Vol. 18, No. 7, 1980, pp. 747–753.
doi:10.2514/3.50815

[45] Munday, P. M., Taira, K., Suwa, T., Numata, D., and Asai, K., "Nonlinear Lift on a Triangular Airfoil in Low-Reynolds-Number Compressible Flow," *Journal of Aircraft*, Vol. 52, No. 3, 2015, pp. 924–931.
doi:10.2514/1.C032983

[46] Okamoto, M., Yasuda, K., and Azuma, A., "Aerodynamic Characteristics of the Wings and Body of a Dragonfly," *The Journal of Experimental Biology*, Vol. 199, No. 2, 1996, pp. 281–294

[47] Pelletier, A., and Mueller, T. J., "Low Reynolds Number Aerodynamics of Low-Aspect-Ratio, Thin/Flat/Cambered-Plate Wings," *Journal of Aircraft*, Vol. 37, No. 5, 2000, pp. 825–832.
doi:10.2514/2.2676

[48] Anyoji, M., Nose, K., Ida, S., Numata, D., Nagai, H., and Asai, K., "Low Reynolds number airfoil testing in a Mars wind tunnel," *40th Fluid Dynamics Conference and Exhibit*, 2010, p. 4627.
doi:10.2514/6.2010-4627

[49] Anyoji, M., Numata, D., Nagai, H., and Asai, K., "Effects of Mach Number and Specific Heat Ratio on Low-Reynolds-Number Airfoil Flows," *AIAA Journal*, Vol. 53, No. 6, 2014, pp. 1640–1654.
doi:10.2514/1.J053468

[50] Suwa, T., Nose, K., Numata, D., Nagai, H., and Asai, K., "Compressibility Effects on Airfoil Aerodynamics at Low Reynolds Number," *30th AIAA Applied Aerodynamics Conference*, AIAA Paper 2012-3029, 2012.
doi:10.2514/6.2012-3029

[51] Chapman, D. R., Kuehn, D. M., and Larson, H. K., "Investigation of separated flows in supersonic and subsonic streams with emphasis on the effect of transition," NACA-TR-1356, 1958.

[52] Sigurdson, L. W., and Roshko, A., "The structure and control of a turbulent reattaching flow," *Turbulence Management and Relaminarisation*, Springer, 1988, pp. 497–514.
doi:10.1007/978-3-642-83281-9_34

[53] Dovgal, A. V, and Sorokin, A. M., "Instability of a laminar separation bubble to vortex shedding," *Thermophysics and Aeromechanics*, vol. 8, 2001, pp. 179–186.

[54] Werlé, H., *Le tunnel hydrodynamique au service de la recherche aérospatiale*, Office National d'Études et de Recherches Aérospatiales, Chatillon, France, 1974, pp. 42–43.

[55] Van Dyke, M., *An Album of Fluid Motion*, The Parabolic Press, Stanford, CA, 1982, pp. 24–26.

[56] Zhou, Y., Alam, M. M., Yang, H. X., Guo, H., and Wood, D. H., "Fluid forces on a very low Reynolds number airfoil and their prediction," *International Journal of Heat and Fluid Flow*, vol. 32, 2011, pp. 329–339.

doi:10.1016/j.ijheatfluidflow.2010.07.008

[57] Yang, Z., and Voke, P. R., "Large-eddy simulation of boundary-layer separation and transition at a change of surface curvature," *Journal of Fluid Mechanics*, vol. 439, 2001, pp. 305–333.

doi:10.1017/S0022112001004633

[58] Levy, D.-E., and Seifert, A., "Simplified dragonfly airfoil aerodynamics at Reynolds numbers below 8000," *Physics of Fluids*, vol. 21, 2009, p. 71901.

doi:10.1063/1.3166867

[59] Kesel, A. B., "Aerodynamic characteristics of dragonfly wing sections compared with technical aerofoils," *Journal of Experimental Biology*, vol. 203, 2000, pp. 3125–3135.

[60] Jongerius, S. R., and Lentink, D., "Structural analysis of a dragonfly wing," *Experimental Mechanics*, vol. 50, 2010, pp. 1323–1334.

doi:10.1007/s11340-010-9411-x

[61] Lentink, D., and de Kat, R., "Gliding swifts attain laminar flow over rough wings," *PloS one*, vol. 9, 2014.

doi:10.1371/journal.pone.0099901

[62] van Bokhorst, E., de Kat, R., Elsinga, G. E., and Lentink, D., "Feather roughness reduces flow separation during low Reynolds number glides of swifts," *Journal of Experimental Biology*, vol. 218, 2015, pp. 3179–3191.

[63] Elimelech, Y., and Ellington, C. P., "Analysis of the transitional flow field over a fixed hummingbird wing," *Journal of Experimental Biology*, vol. 216, 2013, pp. 303–318.

[64] Coello, C. A. C., "A comprehensive survey of evolutionary-based multiobjective optimization techniques," *Knowledge and Information systems*, vol. 1, 1999, pp. 269–308.

doi:10.1007/BF03325101

[65] Srinivas, N., and Deb, K., "Muiltiobjective optimization using nondominated sorting in genetic algorithms," *Evolutionary computation*, vol. 2, 1994, pp. 221–248.

doi:10.1162/evco.1994.2.3.221

[66] Deb, K., Agrawal, S., Pratap, A., and Meyarivan, T., "A fast elitist non-dominated sorting genetic algorithm for multi-objective optimization: NSGA-II," *International conference on parallel problem solving from nature*, Springer, 2000, pp. 849–858.

doi:10.1007/3-540-45356-3_83

[67] Fonseca, C. M., and Fleming, P. J., "Genetic Algorithms for Multiobjective Optimization: Formulation, Discussion, and Generalization.," *University of Sheffield*, 1993, pp. 416–423.

[68] Holst, T. L., and Pulliam, T. H., "Evaluation of Genetic Algorithm Concepts Using Model Problems. Part 2; Multi-Objective Optimization," NASA/TM-2003-212813, 2003.

[69] Pulliam, T., Nemec, M., Holst, T., and Zingg, D., "Comparison of evolutionary (genetic) algorithm and adjoint methods for multi-objective viscous airfoil optimizations," *41st Aerospace Sciences Meeting and Exhibit*, 2003, p. 298.

doi:10.2514/6.2003-298

[70] Deb, K., "Multi-objective optimisation using evolutionary algorithms: an introduction," *Multi-objective evolutionary optimisation for product design and manufacturing*, Springer, 2011, pp. 3–34.

doi:10.1007/978-0-85729-652-8_1

[71] Michalewicz, Z., *Genetic algorithms + data structures= evolution programs*, Springer Science & Business Media, 2013.

[72] Haupt, R. L., and Ellen Haupt, S., "Practical genetic algorithms," 2004.

[73] Pulliam, T., "High order accurate finite-difference methods: as seen in OVERFLOW," *20th AIAA Computational Fluid Dynamics Conference*, 2011, p. 3851.

[74] Holland, J. H., and Goldberg, D., "Genetic algorithms in search, optimization and machine learning," *Massachusetts: Addison-Wesley*, 1989.

[75] Holst, T. L., and Pulliam, T. H., "Evaluation of Genetic Algorithm Concepts using Model Problems. Part 1; Single-Objective Optimization," 2003.

[76] Stone, M. C., and DeRose, T. D., "A geometric characterization of parametric cubic curves," *ACM Transactions on Graphics (TOG)*, vol. 8, 1989, pp. 147–163.

[77] Rumsey, C. L., and Spalart, P. R., "Turbulence Model Behavior in Low Reynolds Number Regions of Aerodynamic Flowfields," *38th AIAA Fluid Dynamics Conference and Exhibit*, Seattle, WA: American Institute of Aeronautics and Astronautics, 2009, p. 5.

doi:10.2514/1.39947

[78] Spalart, P., and Allmaras, S., "A one-equation turbulence model for aerodynamic flows," *30th Aerospace Sciences Meeting and Exhibit*, American Institute of Aeronautics and Astronautics, 1992.

doi:10.2514/6.1992-439

[79] Coder, J. G., and Maughmer, M. D., "Computational fluid dynamics compatible transition modeling using an amplification factor transport equation," *AIAA Journal*, vol. 52, 2014, pp. 2506–2512.

doi:10.2514/1.J052905

[80] Drela, M., "XFOIL: An Analysis and Design System for Low Reynolds Number Airfoils," *Low-Reynolds Number Aerodynamics*, 1989.

[81] Chan, W. M., Rogers, S. E., Nash, S. M., Buning, P. G., Meakin, R. L., Boger, D. A., and Pandya, S., "Chimera Grid Tools User's Manual, Version 2.0," *NASA Ames Research Center*, 2007.

[82] Buning, P. G., and Pulliam, T. H., "Near-body grid adaption for overset grids," *46th AIAA Fluid Dynamics Conference*, 2016, p. 3326.
doi:10.2514/6.2016-3326

[83] Drela, M., "MISES implementation of modified Abu-Ghannam/Shaw transition criterion (second revision)," *Massachusetts Institute of Technology Dept. of Aeronautics and Astronautics*, 1998.

[84] Wooton, R. J., Evans, K. E., Herbert, R., and Smith, W., "Morphology and operation of the locust hind wing," *J. Exp. Biol*, vol. 203, 2000, p. 2921.

[85] Wakeling, J. M., and Ellington, C. P., "Dragonfly flight. I. Gliding flight and steady-state aerodynamic forces.," *Journal of Experimental Biology*, vol. 200, 1997, pp. 543–556.

[86] Rees, C. J. C., "Form and function in corrugated insect wings," *Nature*, vol. 256, 1975, p. 200.
doi:10.1038/256200a0